Document Version
Final published version

Citation (APA)
Liang, M., Fang, Y., Guo, W., He, C., Schlangen, E., Šavija, B., & Contera, S. (2026). Deep active sequential learning of stress evolution in early-age concrete informed by thermo-chemo-mechanical modelling. *Engineering Applications of Artificial Intelligence*, *177*, Article 114985. https://doi.org/10.1016/j.engappai.2026.114985

Engineering Applications of Artificial Intelligence 177 (2026) 114985

Contents lists available at ScienceDirect

Engineering Applications of Artificial Intelligence

journal homepage: www.elsevier.com/locate/engappai

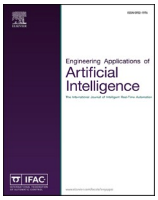

Deep active sequential learning of stress evolution in early-age concrete informed by thermo-chemo-mechanical modelling

Minfei Liang [a,b], Yong Fang [a,*], Wenqi Guo [a], Chuan He [a], Erik Schlangen [c], Branko Šavija [c,**], Sonia Contera [b]

[a] Key Laboratory of Transportation Tunnel Engineering, Ministry of Education, Southwest Jiaotong University, Chengdu, 610031, Sichuan, China
[b] Clarendon Laboratory, Department of Physics, University of Oxford, Oxford, OX1 3PU, UK
[c] Microlab, Faculty of Civil Engineering and Geosciences, Delft University of Technology, Delft, 2628CN, the Netherlands

ARTICLE INFO

Keywords:
Machine learning
Deep learning
Concrete
Early-age cracking
Finite element methods

ABSTRACT

This study presents an integrated finite-element–machine-learning framework for predicting early-age stress evolution in concrete materials/structures by combining an enhanced thermo-chemo-mechanical (TCM) model, deep sequential learning (DSL), and active learning (AL). The proposed TCM model incorporates experimentally informed viscoelasticity, a stable exponential creep–relaxation conversion, and an efficient exponential algorithm for the Maxwell-chain formulation in finite element analysis, which is further validated by a temperature stress testing machine. This model generates high-fidelity stress–time data across diverse mixtures, temperatures, and structural configurations. These simulations are used to train a Gated Recurrent Unit with Monte Carlo Dropout (GRU-MCD) model, whose predictive performance surpasses conventional point-wise approaches such as Light Gradient Boosting Machine and Gaussian Process Regression, yielding higher accuracy with reduced overfitting. The AL strategy further enhances efficiency by enabling the GRU-MCD model to achieve the accuracy of ~900 Latin Hypercube samples using only ~200 samples selected by active learning. Although demonstrated on a wall–base structure, the proposed framework is general and applicable to other cementitious material or structural systems, providing an effective tool for cracking-risk evaluation, reliability analysis, and the design of low-carbon concrete structures.

1. Introduction

Early age cracking (EAC) has long been a critical concern for the durability, functionality, and aesthetics of concrete structures (Fig. 1) (Bentz, 2008), which today remain the most widely used construction materials worldwide. EAC arises from the combined effects of material behavior, structural restraint, and environmental conditions (Fig. 2 (a) (Liang et al., 2024a)). This mechanism can be illustrated by the common case of casting a new concrete wall on an existing concrete base (Fig. 2 (b)). During the construction, the new concrete, i.e., early-age concrete, undergoes hydration reaction in certain temperature and humidity conditions, leading to volumetric deformation (autogenous, thermal, and drying deformation) and the progressive development of mechanical properties. The old concrete base forms restraint against these deformations, generating early-age stresses (EAS) that may exceed the tensile strength and induce cracking (Fig. 2 (c)). Consequently, EAS—resulting from the interaction of material evolution, environmental influences, and structural restraint—serves as a key and direct indicator for assessing EAC risk.

Multi-physics modeling provides a rigorous theoretical framework for EAC simulation, which is essentially the interaction among hydration kinetics, heat transfer, and viscoelastic behavior. Faria et al. (2006) developed a thermo-mechanical model to simulate heat generation, material property evolution, and EAS in restrained concrete slabs, producing results that correlated well with in-situ observations. Azenha et al. (2011) established a thermo-hygro-mechanical framework to account for EAS induced by thermal and drying deformation in concrete slabs subjected to external loads. Zhao et al. (2021) proposed a coupled

---

This article is part of a special issue entitled: Data & AI-CBMS EGE: Jinjun Xu published in Engineering Applications of Artificial Intelligence.

* Corresponding author.

** Corresponding author.

E-mail addresses: minfei.liang@physics.ox.ac.uk (M. Liang), fy980220@swjtu.cn (Y. Fang), swjtuguowenqi@163.com (W. Guo), chuanhe21@swjtu.edu.cn (C. He), Erik.Schlangen@tudelft.nl (E. Schlangen), B.Savija@tudelft.nl (B. Šavija), Sonia.AntoranzContera@physics.ox.ac.uk (S. Contera).

https://doi.org/10.1016/j.engappai.2026.114985
Received 8 January 2026; Received in revised form 19 March 2026; Accepted 26 April 2026
Available online 30 April 2026

Fig. 1. Early-age cracking causing leakage in water-retaining concrete walls.

hygro-thermo-chemo-mechanical model to simulate the mechanical behavior of early-age concrete under varying temperature and humidity conditions. Liang et al. (2022a) also developed a thermo-chemo-mechanical (TCM) model combining Arrhenius' equation for hydration kinetics, Fourier's law for heat transfer, and the exponential algorithm for Kelvin chain-based creep to simulate the viscoelastic evolution of EAS. Recently, a similar TCM framework has been adopted by Li et al. (Li and Wang, 2025) based on the phase field method. These modelling efforts present a significant advancement in understanding EAS evolution. Nevertheless, a critical aspect of such models is creep and relaxation, which is significant in early-age concrete modelling (Liang et al., 2022b; Azenha et al., 2021; Wei et al., 2017). Unfortunately, such effects are often underrepresented or even neglected due to the experimental challenges of characterizing early-age viscoelasticity, potentially compromising the prediction accuracy. The early-age creep test often requires a repeated in-situ loading scheme to continuously measure the creep of the materials at different ages (Irfan-ul-Hassan et al., 2016), which can then establish the full creep compliance function that can be used as the input of the viscoelastic model in the TCM framework (Liang et al., 2024b). Such input is essential for studying and validating the viscoelastic modelling but is often neglected in TCM models for EAS.

Another challenge facing the TCM modelling is the computational cost, which limits their use for extensive optimization and uncertainty quantification in EAC risk analysis. Machine Learning (ML) based modelling has emerged as a promising solution to build efficient surrogates to accelerate complex and expensive physical. Ensemble models, leveraging the bootstrap or boosting strategies combining weak learners such as decision trees models (Breiman, 1996; Chen and Guestrin, 2016; Ke et al., 2017), have been successfully applied to predict engineering properties of concrete, including compressive strength (Wan et al., 2021; Nguyen et al., 2021), flexural strength (Kang et al., 2021), surface chloride concentration (Cai et al., 2020), elastic modulus (Han et al., 2020), and creep (Liang et al., 2022c). In many of these studies, ensemble learning models were further combined with SHapley Additive exPlanations (SHAP) to provide not only accurate predictions of engineering properties, but also interpretable insights that are consistent with the underlying physical mechanisms (Xu et al., 2025; Zhang et al., 2026a). In addition, some recent studies have also focused on optimization algorithms, such as metaheuristic and Bayesian optimization, to further improve the performance of ensemble learning models in concrete-related predictions (Zhang et al., 2025a, 2025b).

The ML-based modelling for EAC risk analysis remains scarce, potentially due to the complexity of the experiment and modeling of EAS that results in the lack of training data. Based on the TCM model, Liang et al. (2022a) used a Light Gradient Boosting Machine (LGBM) to predict the EAS of a TSTM specimen. Recently, using datasets from thermal-mechanical models, Do et al. (Do and Le, 2024) trained ML models such as Extreme Gradient Boosting (XGB) and Gaussian Process (GP) to predict the cracking potential and cracking time of concrete piers with different cross-sectional dimensions, temperatures, etc. Despite the effectiveness of these models, the EAS is inherently a time-dependent behavior while currently the models used are for single point prediction. As a result, they may not fully capture the evolution of the EAS process over time. Another limitation that restrains the development of these models is the scarcity of data, largely due to the high numerical cost of running coupled multi-field simulations. Recent studies have attempted to mitigate data scarcity through synthetic data augmentation (Liu et al., 2026) and transfer learning (Fan et al., 2026). However, both strategies generally rely on a sufficient amount of experimental data to generate reliable synthetic samples or to establish a transferable

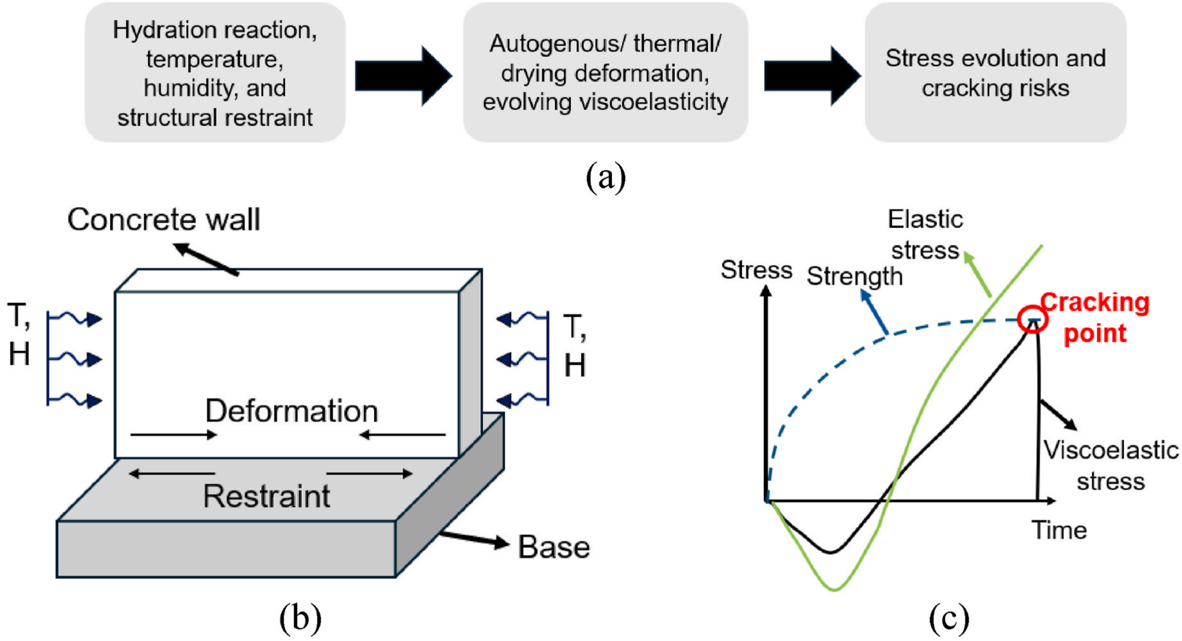

Fig. 2. General mechanism of early-age cracking (EAC): (a) influencing factors and stress evolution; (b) a new concrete wall restrained by an old concrete base; and (c) occurrence of EAC when early-age stress (EAS) exceeds the tensile strength.

baseline model. For EAS prediction, such a prerequisite is difficult to satisfy because the relevant experimental data are extremely limited, while high-fidelity FE simulations are themselves too computationally expensive to provide large datasets efficiently.

To sum up, current research on ML-enhanced EAS prediction faces three major challenges: 1) limited verification of stress relaxation modelling within the multifield models, 2) incompatibility between the time-dependent nature of EAS and the single-point prediction capability of most used machine learning models, and 3) scarcity of EAS data due to the high computational cost of multi-field simulations. This paper will contribute accordingly by proposing 1) A TCM model featuring an improved and validated stress relaxation computation method; 2) A deep sequential learning (DSL) framework that integrates material and structural information to predict the entire EAS evolution curve; 3) An active learning strategy that enables the DSL model to achieve high accuracy with a limited training dataset, thereby reducing the reliance on computationally expensive multifield simulations.

2. Thermo-chemo-mechanical modelling

This section details the TCM modelling approach, its experimental verification, and the implementation of the finite element models, which together form the basis for constructing the database used for training machine learning models.

2.1. Theory

The adopted TCM framework in this study is shown in Fig. 3. Consistent with previous studies (Zhao et al., 2020, 2021; Di Luzio and Cusatis, 2009a, 2009b), Fourier's law is used for heat transfer and Arrhenius's equation for hydration kinetics. These constitutive relations are adopted to simulate the thermo- and chemo-fields, which are fully coupled through temperature and hydration degree: the temperature output from the thermo-field enters the exponential term of the hydration kinetics, while the hydration degree contributes to the heat source term of the thermo-field. The material model combines an XGBoost-based compressive strength predictor with an adjusted Model Code 2010 (MC, 2010) formulation (Liang et al., 2022a; Wan et al., 2021; Liang et al., 2022c; International Federation for Structural Concrete (fib), 2013). The predicted strength serves as input to MC 2010 to compute shrinkage, creep compliance, and elastic modulus, which can be fed into the mechanical field of the TCM model.

A critical aspect of the multifield model is the validity of the visco-elastic stress evolution process. Herein, the TCM model improves the mechanical field with a 9-unit Maxwell chain model, informed by an exponential conversion from creep to relaxation and validated by hourly repeated creep tests and TSTM tests (Liang et al., 2024b, 2024c). Using the outputs from the material model and the thermo-chemo fields, the mechanical field predicts the early-age stress (EAS) evolution as a 672×1 vector, which is subsequently used for machine learning training.

2.1.1. Chemo- field

When cement contacts with water, unhydrated clinker phases—C_3S, C_2S, C_3A, and C_4AF—react with free water to form calcium silicate hydrate (C–S–H), calcium hydroxide (CH), ettringite (Aft), and monosulfate (Afm) (Taylor, 1997). In this paper, hydration reaction is treated as a global process, consistent with existing multifield models (Di Luzio and Cusatis, 2009a, 2009b; Cervera et al., 1999a; Gawin et al., 2006a, 2006b). Assuming hydration kinetics are governed by Gibbs free energy depending on temperature and hydration degree, the reaction rate follows an Arrhenius-type law (Di Luzio and Cusatis, 2009a; Ulm and Coussy, 1995; Cervera et al., 1999b):

$$\dot{\alpha} = A(\alpha)e^{-\frac{E_{ac}}{RT}} \tag{1a}$$

$$A(\alpha) = A_1\left(\frac{A_2}{\alpha_{ult}} + \alpha\right)(\alpha_{ult} - \alpha)e^{-\eta\frac{\alpha}{\alpha_{ult}}} \tag{1b}$$

where α is the hydration degree, $\dot{\alpha}$ its time derivative, E_{ac} the apparent activation energy, R the gas constant, T the temperature, and A_1, A_2, η cement-specific parameters calibrated from adiabatic tests (Di Luzio and Cusatis, 2009a). The ultimate hydration degree α_{ult} depends on the water-to-cement ratio w/c (Pantazopoulou and Mills, 1995):

$$\alpha_{ult} = \frac{1.031w/c}{0.194 + w/c} \tag{2}$$

Three parameter sets (A_1,A_2,η) are used for the SL, N, and R cement classes defined by MC 2010 (see Section 2.3) (International Federation for Structural Concrete (fib), 2013). The apparent activation energy E_{ac} is temperature- and cement-dependent, decreasing below 20 °C and constant above (van Breugel, 1991), following the bilinear relationship (Hansen and Pedersen, 1977):

$$E_{ac} = \begin{cases} E_{ac,0}, if\ T \geq 20^{\circ}C \\ E_{ac,0} + 1470(20 - T), if\ T < 20^{\circ}C \end{cases} \tag{3}$$

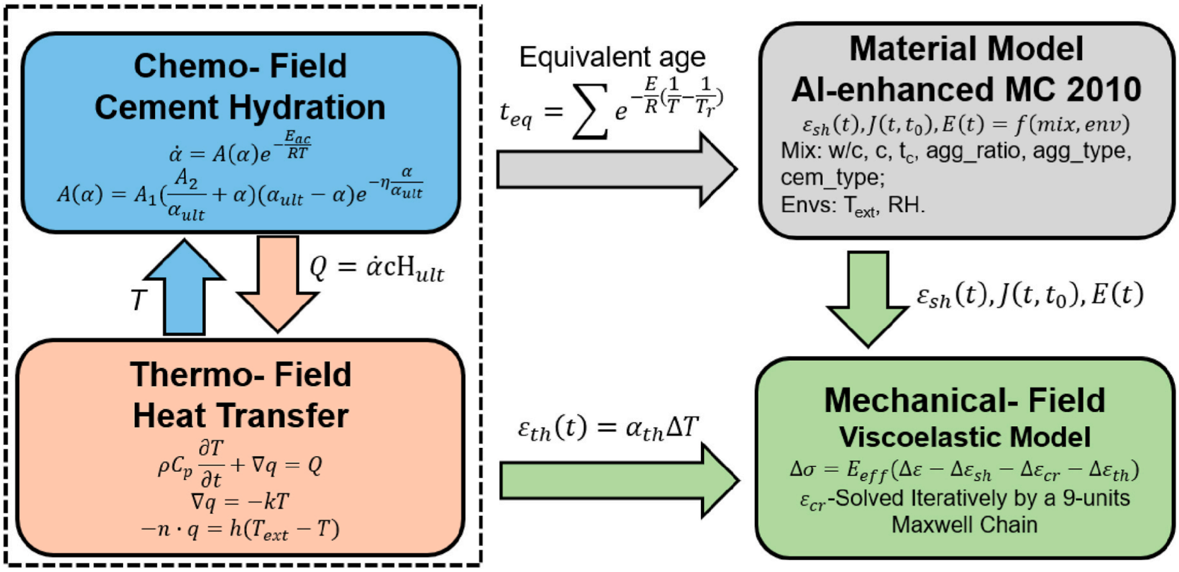

Fig. 3. Framework of the thermo-chemo-mechanical modelling.

where $E_{ac,0}$ is the activation energy at 20 °C. At each time step, the computed hydration degree α provides the heat source term for the thermo-field.

2.1.2. Thermo- field

For temperatures below 100 °C, heat transfer in concrete follows Fourier's law (Hansen and Pedersen, 1977):

$$\rho C_p \frac{\partial T}{\partial t} + \nabla q = \dot{Q} \tag{4a}$$

$$\nabla q = -k \nabla T \tag{4b}$$

$$-n \cdot q = h(T_{ext} - T) \tag{4c}$$

where ρ is the concrete density, C_p the specific heat, k the thermal conductivity, q the heat flux, and h the heat transfer coefficient. Eq. (4c) describes the convective heat flux at the surface, where n is the outward normal and T_{ext} the ambient temperature. The internal heat source $\dot{Q}$ in Eq. (4a) represents heat released by cement hydration and is calculated from the chemo-field hydration degree (Cervera et al., 1999b):

$$\dot{Q} = \dot{\alpha} c Q_{ult} \tag{5}$$

where c is the cement mass and Q_{ult} the ultimate hydration heat per unit cement mass, typically 400–550 kJ/kg (Bazant and Kaplan, 1996). Three sets of Q_{ult} values are used in this study to represent different cement types (see Section 2.3). The resulting temperature field directly affects the hydration kinetics (Eq. (1a)), ensuring full coupling between thermo- and chemo-fields.

The thermo-field provides important input to the mechanical field. The temperature variation induces thermal deformation, expressed as:

$$\varepsilon_{th}(t) = \alpha_{th} \Delta T \tag{6}$$

where α_{th} is the linear coefficient of thermal expansion (a constant value of 1.0×10^{-5} [1/K] is adopted herein (Bentz, 2008)). Although α_{th} may vary slightly at very early age (before 48 h), it becomes relatively stable afterwards. Since the concrete stiffness is still low and creep-relaxation is strong during this earliest period, the influence of this simplification on the final stress prediction is expected to be limited (Liang, 2024). The temperature history also determines the equivalent age of the concrete t_{eq}, expressed as (Hansen and Pedersen, 1977):

$$t_{eq} = \sum e^{-\frac{E_{ac}}{R}\left(\frac{1}{T} - \frac{1}{T_r}\right)} \tag{7}$$

where T_r is the reference temperature (20 °C). The equivalent age t_{eq} will be used to query the evolution of viscoelastic properties and strength of the material given different temperature histories.

2.1.3. Mechanical- field

Different from the thermo- and chemo-fields, which have been validated by abundant experimental evidence and extended to different application cases, the mechanical field for the viscoelastic process of EAS evolution is more unclear and has been extensively studied by many researchers (Wei et al., 2017; Klausen, 2016; Liu and Schindler, 2020; Shen et al., 2017; Azenha et al., 2017). Assuming early-age concrete as an evolving viscoelastic solid whose deformation is restrained (Azenha et al., 2021), its EAS can be expressed by the Volterra integral as below:

$$\sigma(t) = \int_0^t R(t_0, t) \mathrm{d}\varepsilon(t_0) \tag{8}$$

where σ is the EAS, R the relaxation modulus, ε the deformation that is restrained, t_0 the time when the deformation is restrained, t the total duration of the EAS. A key challenge in studying EAS evolution is the limited data on the viscoelastic properties of early-age concrete. Creep tests are usually preferred because relaxation tests are very costly and technically demanding, requiring precise strain control and accounting for restrained shrinkage stress. In contrast, creep tests are simpler, as deformation from autogenous shrinkage can be directly measured and subtracted using a dummy specimen. However, even when the creep compliance function $J(t_0, t)$ is obtained, converting it into the relaxation modulus required in Eq. (8) is still nontrivial. For a constant unit strain in a relaxation test, with stress $\sigma(t)$ applied from t_0 to t_f, the creep compliance J and relaxation modulus R satisfy the Volterra integral equation:

$$J(t_0, t_f) R(t_0, t_0) + \int_{t_{0+}}^{t_f} J(t', t_f) R(\dot{t_0}, t') \mathrm{d}t' = 1 \tag{9}$$

However, due to the strong non-linearity of aging creep and relaxation, the numerical solution of Eq. (9) may yield negative values of the relaxation modulus (Liang et al., 2024c). This is physically unacceptable, because the relaxation modulus should remain positive so that compressive strain produces compressive stress and tensile strain produces tensile stress. Otherwise, the calculated stress response may reverse sign and lead to non-physical results. Therefore, directly inverting the creep compliance through the Volterra integral equation may introduce numerical instability in early-age stress analysis. In view of this issue, this paper adopts the exponential conversion formula proposed by Wittmann and van Breugel (Wittmann, 1974; Van Breugel, 1980), as below:

$$R(t_0, t) = e^{1 - J(t_0, t) E(t_0)} E(t_0) \tag{10}$$

This expression assumes that $R(t_0, t)$ follows an exponential decay form, which guarantees positivity of the relaxation modulus and avoids the numerical instability of direct inversion. It has been successfully applied to model EAS in both ordinary Portland cement concrete and alkali-activated slag concrete (Ulm and Coussy, 1995; Boulay et al., 2014). Nevertheless, Eq. (10) is a simplified approximation derived specifically for early-age relaxation. Although it preserves positivity and improves numerical robustness, it may deviate from the exact Volterra relation in long-term relaxation analysis and may therefore overestimate the relaxation effect when applied beyond the early-age range (Ulm and Coussy, 1995).

Obtaining the creep compliance from experiments, one can use Eq. (10) to convert the measured creep compliance into the relaxation modulus, which then serves as the input for stress relaxation (Eq. (8)). However, a major challenge with Eq. (8), particularly when solving it numerically in finite element (FE) analysis, is the need to store and repeatedly access the entire history of strain increments $\mathrm{d}\varepsilon(t_0)$ at every integration point and time step. This results in a substantial memory demand and high computational cost, significantly slowing down FE analysis. To address this issue, this paper adopts the exponential algorithm to simulate stress relaxation. This approach transforms the Volterra integral into a rate-type formulation, thereby eliminating the need to store the full strain history (Bažant and Jirásek, 2018; Bazant and Wu, 1974; Di Luzio et al., 2020). First, Eq. (8) is rewritten in incremental form under the assumption that strain increments are linear within each time interval:

$$\Delta\sigma = E^* (\Delta\varepsilon - \Delta\varepsilon_{ad}) - \sigma^* \tag{11a}$$

where the $\Delta\varepsilon_{ad}$ is the autogenous, thermal, and drying deformation that induces EAS. The effective modulus E^* and the history term σ^* can be expressed as:

$$E^* = \frac{\int_t^{t+\Delta t} R(t_0, t + \Delta t) dt_0}{\Delta t} \tag{11b}$$

$$\sigma^* = \int_0^t [R(t_0, t + \Delta t) - R(t_0, t)] \dot{\varepsilon}(t_0) dt_0 \tag{11c}$$

For each loading age t_0, the relaxation function $R(t_0, t)$ of concrete is approximated by a series of n-unit Maxwell chains. The creep function is first obtained from experiments and then converted into the corresponding relaxation modulus. The parameters $\left(E_j, \mu_j\right)$ of the Maxwell chain are subsequently identified by nonlinear fitting in MATLAB for each loading age separately. The fitted Maxwell chain (with R^2 values close to 1.0) is then used as the material input in the subsequent FE analysis:

$$R(t_0, t) = E_0(t_0) + \sum_{j=1}^{n} E_j(t_0) e^{-\frac{t-t'}{\mu_j}} \tag{12}$$

Substituting Eq. (12) into Eq. (11) and applying midpoint rule for time discretization, the following recursive expressions for E^* and σ^* are obtained:

$$E^*(t^*) = \sum_{j=1}^{N} E_j(t^*) \left(1 - e^{-\frac{\Delta t}{\mu_j}}\right) \frac{\mu_j}{\Delta t} + E_0(t^*) \tag{13a}$$

$$\sigma^*(t_i) = \sum_{j=1}^{n} \left(1 - e^{-\frac{\Delta t}{\mu_j}}\right) \sigma_j^*(t_i) \tag{13b}$$

$$\sigma_j^*(t_{i+1}) = e^{-\frac{\Delta t}{\mu_j}} \sigma_j^*(t_i) + E^*(t^*) \left(1 - e^{-\frac{\Delta t}{\mu_j}}\right) \frac{\mu_j}{\Delta t} (\Delta\varepsilon(t_i) - \Delta\varepsilon_{ad}(t_i)) \tag{13c}$$

This recursive formulation enables an efficient step-by-step update of the stress state, avoiding the need to store the entire strain history and thus reducing both memory consumption and computational cost.

2.2. Experimental verification

The measurement of EAS provides first-hand data for evaluating the EAC risk and verifying the multifield models. Common EAS measurement methods include the internal restraint test (Semianiuk et al., 2017), rigid cracking frame test (Lura et al., 2009), ring test (Briffaut et al., 2016), and the temperature stress testing machine (TSTM) (Klausen et al., 2019). Among these, the ring test and TSTM have been the most used methods owing to their flexibility and effectiveness. Ring test is often favored over TSTM due to its simplicity, and have been recently applied for studying the EAC risks of basalt-polypropylene fiber reinforced concrete (Mao et al., 2023) and fly ash/slag concrete (Afroz et al., 2022). TSTM, in contrast, is used for more comprehensive evaluations. Its versatile design enables measurement not only of EAS (Liang et al., 2023a) but also EAC-relevant properties, including autogenous and thermal deformation, elastic modulus (Boulay et al., 2014), creep/relaxation behavior (Delsaute et al., 2016), and coefficient of thermal expansion under a customized temperature history and restraint degree (Klausen et al., 2022; Shen et al., 2016), thus providing end-to-end data for EAC risk assessment. However, the complexity of TSTM system significantly increases the testing cost and therefore hinders its wide application. To this end, studies have been performed to improve the system design for better efficiency (Zhu et al., 2017, 2018; Nguyen et al., 2019; Ou et al., 2023). Recently, a Mini-TSTM has been developed for testing above EAC-relevant properties with significantly better efficiency while maintaining similar accuracy compared to conventional TSTM (Liang et al., 2024b), which presents a useful tool for EAC study.

The TCM model proposed above has been validated by extensive TSTM experiments. The calibration and verification of Eqs. (1)–(5) for simulating hydration reaction and heat transfer can be found in (Di Luzio and Cusatis, 2009b). This section focuses on the experimental verification of the mechanical field (Eqs. (6)–(11)) under various temperatures. The developed Mini-TSTM (Liang et al., 2024b) was used as the main testing method for measuring the evolution of viscoelastic properties, EAS, and deformations (Fig. 4). The testing system contains two specimens which both are connected to a water circulation system for temperature control (Fig. 4 (a)). Both specimens are cast in 3D-printed molds that were specially designed to enable in-situ mechanical testing of the early-age material, efficient temperature control, and sensitive strain measurement (Fig. 4 (b)). After casting, one specimen can be placed in a universal testing machine for mechanical testing, and the other can be used as the dummy specimen tested in mechanically free condition to measure the autogenous and thermal deformation.

By applying different mechanical boundaries in the Mini-TSTM tests, important early-age properties can be obtained, including:

1) Autogenous and thermal deformation by measuring the free dummy specimen.
2) Evolution of creep compliance function using an hourly-repeated loading scheme.
3) EAS evolution using a fully restrained loading condition.

Note that these measurements all started from a very early age and covered various temperature conditions, which enabled an end-to-end validation of the TCM model. The tests were performed on cement paste and concrete with different binders and water-cement ratios and can be found in our previous studies (Liang et al., 2022b, 2024c, 2024d; Li et al., 2022). Representative validation results will be discussed in this paper.

2.3. Implementation

2.3.1. Overall workflow and parameter settings

This section describes how the TCM model is implemented to generate the dataset used for training the ML model. We consider a concrete wall cast on an existing base fixed to the ground (Fig. 5(a)). The geometry of the wall–base structure is parameterized and, together with environmental and material inputs, feeds the workflow in Fig. 5(b–c). Material design parameters are first passed to an XGBoost model trained on the NU database (2606 records) to predict the 28-day compressive strength with high accuracy (R^2>0.94) (Liang et al., 2022a; Wan et al., 2021; Hubler et al., 2015). Using the predicted compressive strength along with the material design and environmental conditions, a modified MC 2010 (Liang et al., 2022a; International Federation for Structural Concrete (fib), 2013) provides the required properties—elastic modulus, creep compliance, and free deformation. These outputs, combined with the geometry parameters, constitute the inputs of the TCM model, which then computes the development of EAS. The resulting EAS time series are extracted to build the database for training the downstream ML models.

Exact variable definitions and value ranges for the material mixture design, environmental conditions, and structural geometry are summarized in Table 1. Note that the variables *agg_type* and *cem_type* represent the types of aggregates and cement, following the definition of MC 2010 (International Federation for Structural Concrete (fib), 2013), as shown in Table 2. In the present study, these two variables are represented by numerical indices. Such a treatment is intended to reflect the underlying material properties, with *cem_type* corresponding to increasing cement strength class and *agg_type* corresponding to a trend from denser and stiffer aggregates to relatively less dense ones. Therefore, this numerical representation indicates the physical characteristics of the material classes, which may be beneficial for future model extension and extrapolation. The variable *E_b_ratio* represents the ratio of the 28-day elastic modulus of the wall to that of the base. It should be noted that, in the simulation, the elastic modulus of the wall is gradually ramped from 0 to its 28-day value, whereas the elastic modulus of the base remains constant. Corresponding to different types of cement, the parameters used in thermo-chemo analysis are presented in Table 3 (Di

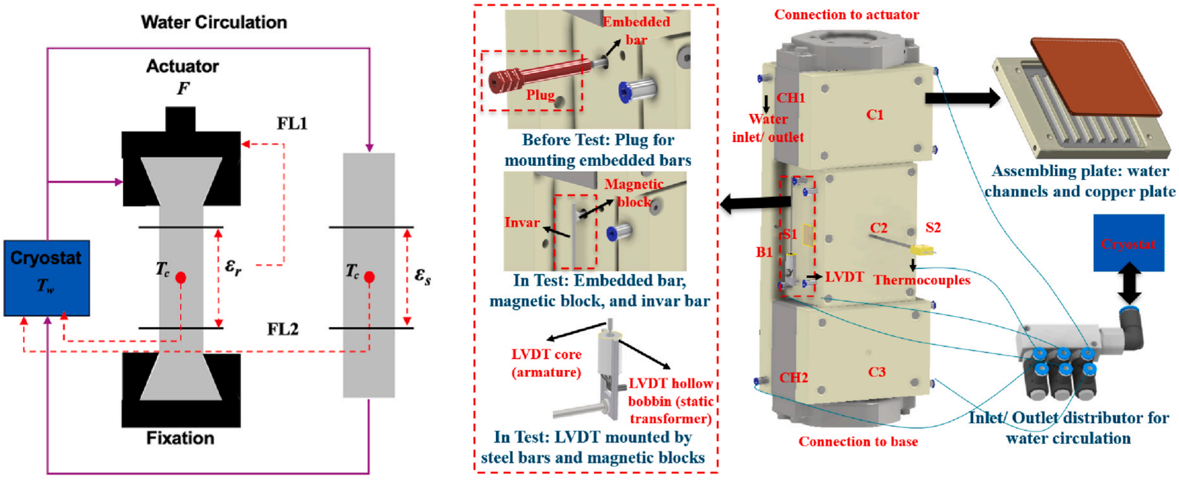

(a) (b)

Fig. 4. The Mini-Temperature Stress Testing Machine (TSTM) (Liang et al., 2024b): (a) TSTM testing principals; (b) Design of the Mini-TSTM.

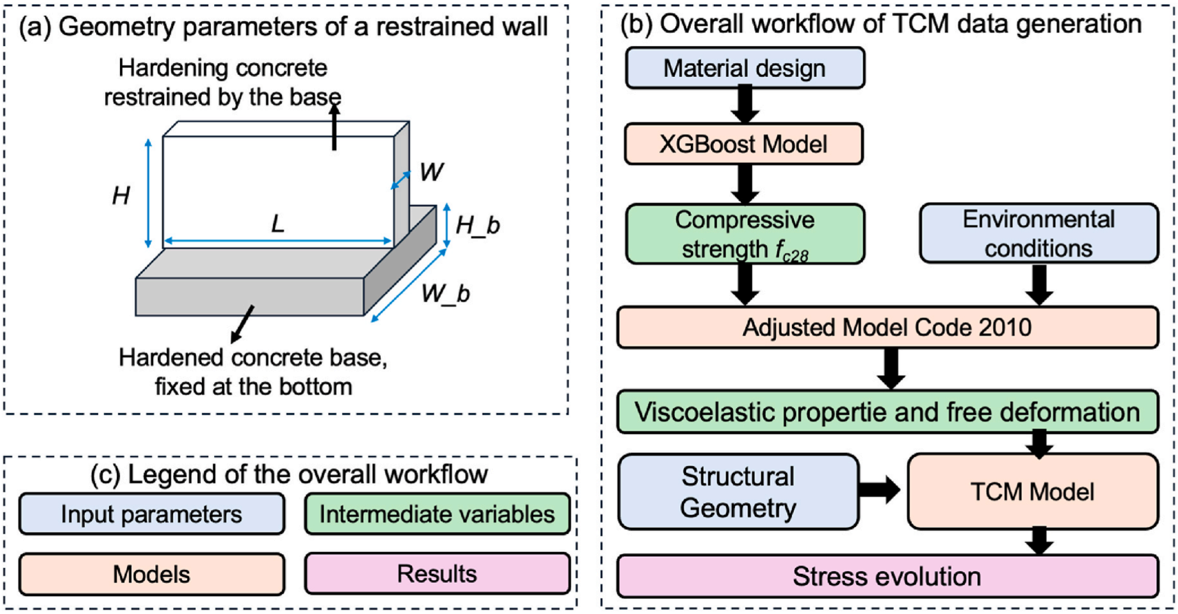

Fig. 5. Implementing the TCM model for generating the dataset.

Luzio and Cusatis, 2009b; Klemczak et al., 2018; Lee et al., 2009). Note that the heat transfer coefficient h is assumed as a constant following the assumption that the wall is covered by curing blanket (Lee et al., 2009).

2.3.2. FE configuration

The TCM model uses the COMSOL Multiphysics platform as the numerical solver. The chemo-field is defined by a domain ordinary differential equation (DODE) according to Eqs. (1) and (2), with the degree of hydration α as the dependent variable. Subsequently, the Heat Transfer Module embedded in COMSOL is directly used for solving the thermo-field as in Eq. (4). The thermo- and chemo-fields are coupled by two variables: 1) both fields share the same temperature field; 2) the source term in the thermo-field is calculated using α from the chemo-field as in Eq. (5).

For the mechanical field, a user-defined material subroutine (Fig. 6) is developed to implement the exponential algorithm for the viscoelastic analysis in the form of Maxwell chains as in Eq. 10–13. We assume a Maxwell chain with 9 units covering the relaxation time μ_j ($j = 1 \sim 9$) ranging from 10^{-4} to 10^{4} hours. Based on the adjusted MC2010 model, the creep compliance function $J(t_0, t)$ can be obtained and then transformed to the relaxation modulus function $R(t_0, t)$ by Eq. (10). Corresponding to each t_0, the parameter of each Maxwell unit $E_j(t_0)$ ($j = 1 \sim 9$) can be obtained by using the nonlinear optimization tool provided by MATLAB (Waltz et al., 2006) to fit the relaxation function of Maxwell chain (Eq. (12)) to the $R(t_0, t)$ obtained by Eq. (10). Afterwards, the Maxwell chain can be imported to the mechanical field to start the viscoelastic analysis.

The developed TCM framework is used to calculate the EAS evolution of a wall-base structure. Hexahedral elements are used to discretize the structure for the FE analysis (Fig. 7). The full TCM formulation, including material evolution and viscoelasticity, is applied to the hardening concrete wall, whereas the base, treated as hardened concrete, is modeled with the thermo-field and linear elasticity. Convective boundary conditions are prescribed on all external surfaces. The bottom surface of the base is fully restrained with zero displacement. The wall is assumed to be bonded to the base; consequently, displacement

Table 1
Variables of the material model.

Category	Variables	Representation	Range
Material design	*cem*	Cement content (kg/m^3)	250-600
	wc	Water to cement ratio	0.2- 0.7
	agg	Aggregate-cement ratio	1.50-9.10
	agg_type	Aggregate type	1, 2, 3, 4
	cem_type	Cement type	1, 2, 3
	t_c	Time of sealed curing (Hours)	7- 168
Environmental conditions	*T_env*	Environmental Temperature (°C)	10- 40
	RH	Relative Humidity	0.2-1.0
Structural geometry	*len*	Length of the wall (m)	6- 20
	width	Width of the wall (m)	0.1- 0.4
	height	Height of the wall (m)	2.5- 6.0
	b_h_ratio	Ratio between base thickness and wall height	0.05-0.4
	E_b_ratio	Ratio of 28-day elastic modulus between the wall and base	0.8- 2.0
	VS	Volume to surface ratio of the wall (mm)	47.5-183.6

Table 2
Definitions of categorical variables.

cem_type	Cement class
1	32.5N
2	32.5R and 42.5 N
3	42.5R, 52.5N, 52.5R
agg_type	**Aggregate content**
1	Basalt, dense limestone
2	Quartzite
3	Limestone
4	Sandstone

Table 3
Parameter settings in the thermo-chemo field for different cement types (Di Luzio and Cusatis, 2009b; Klemczak et al., 2018).

cem_type	Q_{ult} (J/g)	η	A_1	A_2	k (W/(m*K))	h (W/(m^2*K))	C_p (J/(kg*K))
1	400	1.41×10^7	1×10^{-2}	8	2.3	5	
2	439	4×10^7	5×10^{-2}	8.5			1100
3	520	8×10^7	8×10^{-2}	8			

continuity is enforced at the interface. In this case, the wall is indirectly restrained through the finite stiffness of the base. It should be noted that this work does not aim to simulate a specific scenario and therefore simplifies the mechanical and thermal conditions. The fully-restraint condition produces conservative results of the EAS because in reality, as the restraint degree is often less than 1.0 (Klausen et al., 2022). More realistic boundary condition settings for engineering-specific applications are available in (Azenha et al., 2021).

Backward difference method and damped Newton method are adopted to obtain convergent numerical solutions (Hoffman et al., 2018; Stute et al., 2013). The analysis spans 0–672 h (the first 28 days of hardening). The longitudinal stress averaged over the mid-section B–B—which closely coincides with the first principal stress in this case—is extracted and area-averaged to constitute the EAS dataset for ML training.

3. ML for stress evolution

This section details the ML models constructed based on the data provided by the TCM model, which aims to shorten the prediction time limited by the expensive computational cost of the multifield FE analysis.

3.1. Sampling and database

To construct a database that is informative across a broad range of engineering scenarios, while acknowledging limited computational resources, two sampling techniques are employed.

3.1.1. Latin Hypercube Sampling

Latin hypercube sampling (LHS) (Loh, 1996), with the criterion of maximizing the minimum inter-sample distance, is used to generate a sample pool of 1000 points within the bounds listed in Table 1. The sampling is performed with MATLAB's *lhsdesign* using five optimization iterations. Under LHS, the entire database is generated before ML training.

3.1.2. Uncertainty-guided sampling and active learning framework

Another sampling strategy adopted in this study is active learning (AL) driven by uncertainty quantification (Moustapha et al., 2022). Unlike LHS, which is a one-shot space-filling method that generates the entire database before ML training, AL is adaptive: the sample selection evolves based on the model's current predictive performance. While LHS ensures broad coverage of the input space, AL focuses computational resources on the most informative regions, enabling more efficient data acquisition when simulations are expensive.

Compared with LHS, AL is a dynamic procedure that, in each iteration, alternates among TCM simulation, ML training, and uncertainty-guided sample selection (Fig. 8). First, a large candidate set (>50,000 points) is generated as the sample pool. The TCM model is then applied to label the samples to provide data for training. In the first iteration, a small subset is randomly drawn from the pool (64 points in this paper) to initialize AL (Fig. 8(a–c)). Next, the prediction uncertainty over the remaining candidate pool is quantified, enabling an acquisition score to be computed for each unlabeled point (Fig. 8 (d))—e.g., via predictive variance, entropy, or task-specific acquisition functions such as expected improvement (Echard et al., 2011; Tomar and Burton, 2021; Jones et al., 1998). In the present study, the acquisition score is defined as the mean predictive standard deviation of the reconstructed EAS curve over the whole time sequence. The unlabeled samples are then ranked accordingly. The points with the highest acquisition scores are then selected, labeled by the TCM model, and appended to the training set for the next iteration (Fig. 8(e–f)). This process is repeated until the total number of labeled samples reaches 1000. Such a fixed sample stopping criterion is adopted here so that AL and LHS can be compared under the same data budget.

In this paper, the ML model for sequence prediction is a Gated Recurrent Unit with Monte-Carlo Dropout (GRU-MCD). Although GRU-MCD provides predictive uncertainty, its estimates are sensitive to the number of training samples. Therefore, within the AL loop we instead employ a Gaussian process (GP) (Rasmussen and Williams, 2006) as the uncertainty model because of its stable and well-founded probabilistic formulation. In practice, the GRU-MCD is used as the primary predictor for sequence learning, whereas the GP (Rasmussen and Williams, 2006) is trained as an auxiliary uncertainty model for sample acquisition. More specifically, the EAS curves are first represented in the reduced PCA space, and the GP is used to estimate the predictive variance in this reduced output space for each candidate point. The resulting uncertainty is then used to guide sample selection in AL. In this way, the predictor and the acquisition model play different but complementary roles: GRU-MCD is responsible for accurate surrogate prediction, while GP provides a more stable uncertainty estimate for adaptive sampling.

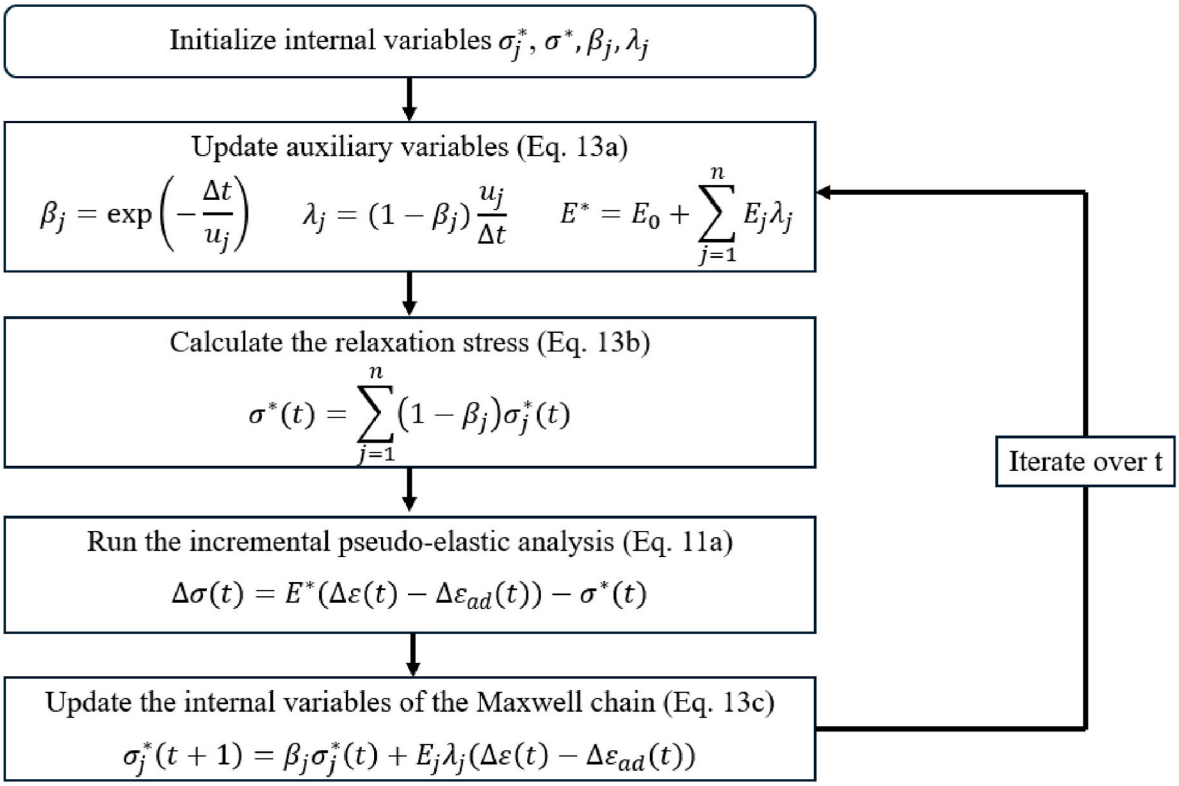

Fig. 6. Workflow of the exponential algorithm for Maxwell chain model.

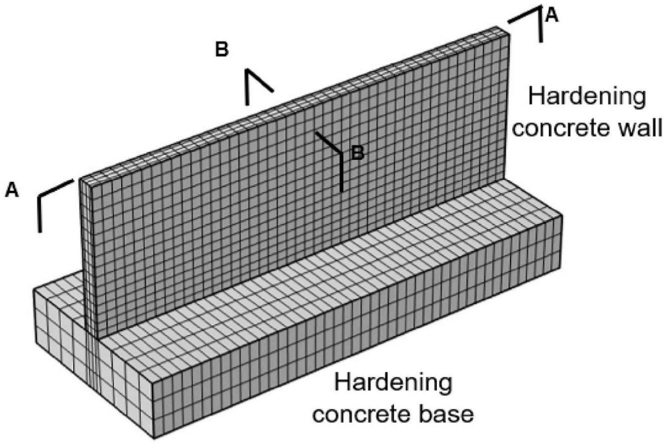

Fig. 7. Mesh of the wall-base structure.

3.2. ML models

This section provides an overview of the ML models used as the surrogate to efficiently predict EAS. Two types of models are presented herein as a comparison: point-wise models and sequence models. Prior to ML modeling, the scalar input features were standardized to zero mean and unit variance. The EAS curves were also standardized and processed via Principal Component Analysis (PCA) (Liang et al., 2022a) to reduce dimensionality by projecting each curve (a 672 × 1 vector) onto a small set of leading principal components (a 10 × 1 vector retaining the majority of variance, as will be shown in Section 4.2). The models were then trained and evaluated in this reduced feature space. In the sequence model, temporal order was encoded through a learnable time embedding rather than being directly used as a raw normalized input.

3.2.1. Point-wise prediction models

Two point-wise prediction models, i.e., Light Gradient Boosting Machine (LGBM) (Ke et al., 2017) and Gaussian Process Regression (GPR) (Rasmussen and Williams, 2006) are used in this study for EAS prediction, as both models have proved to obtain excellent performance in prediction of concrete properties and behaviors (Liang et al., 2022a, 2022c; Wan et al., 2021; Cai et al., 2020; Do and Le, 2024; Bayar and Bilir, 2019).

LGBM is a gradient-boosting decision-tree ensemble: each new weak learner is fit to the residuals of the previous tree ensemble, greedily reducing prediction error. Compared with XGBoost, LGBM attains higher efficiency via a lightweight design featuring histogram-based, leaf-wise growth, gradient-based one-side sampling, and exclusive feature bundling (Ke et al., 2017). On the other hand, GP model function values as a stochastic process in which any finite set is jointly Gaussian. Leveraging this property, GPs provide both predictive means and variance. A GP is specified by its covariance kernel evaluated over pairs of observations; kernel choice reflects desired smoothness and prior structure. Assuming a smooth EAS curve and input variable space, we adopt the radial basis function (RBF) kernel, which is infinitely differentiable and promotes smooth predictions (Rasmussen and Williams, 2006).

Using material design variables, environmental conditions, and structural geometry (Table 1) as inputs, we train 10 independent LGBM and GPR regressors, one for each retained principal component (PC). The predicted PC coefficients are concatenated and inverse-PCA transformed to recover the full EAS vector σ_n ($n = 1 \sim 672\ h$), as illustrated in Fig. 9. The dataset generated via Latin Hypercube Sampling (LHS) is split 70/15/15 into training/validation/testing. The EAS outputs are standardized based on the training set, and PCA is then performed on the standardized training outputs. The input variables are also standardized before regression.

For LGBM, the hyperparameters of each PC-specific regressor are optimized using Optuna with 40 trials, where the objective function is defined as the validation MSE obtained from the validation set. The

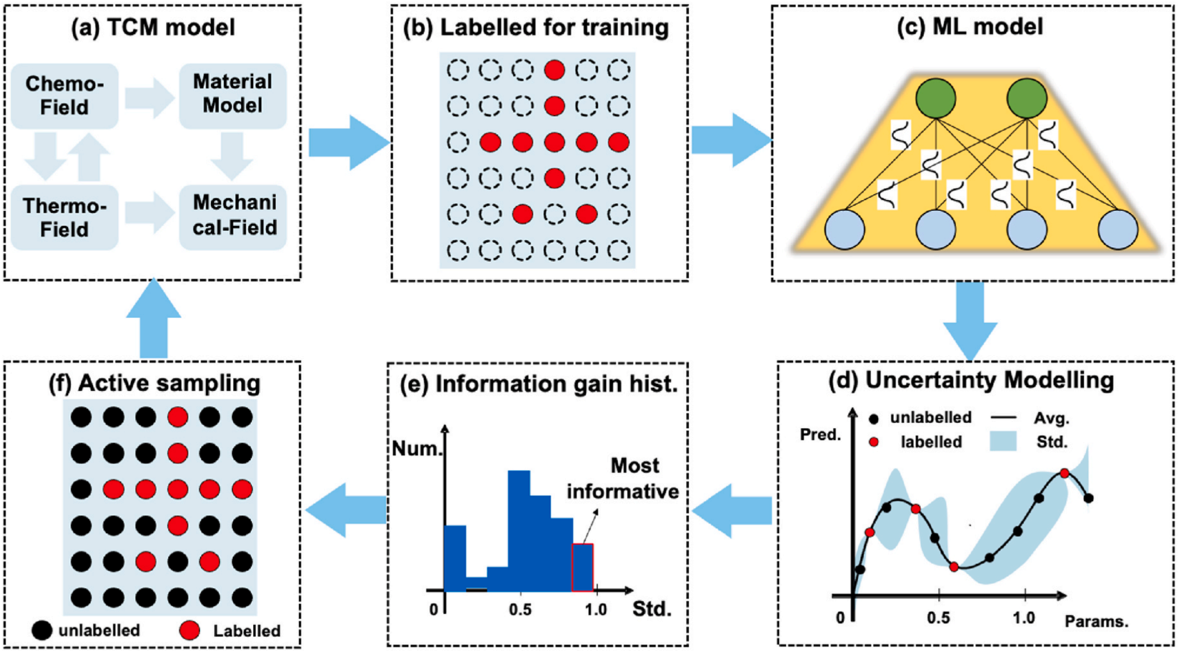

Fig. 8. Uncertainty-guided active learning framework.

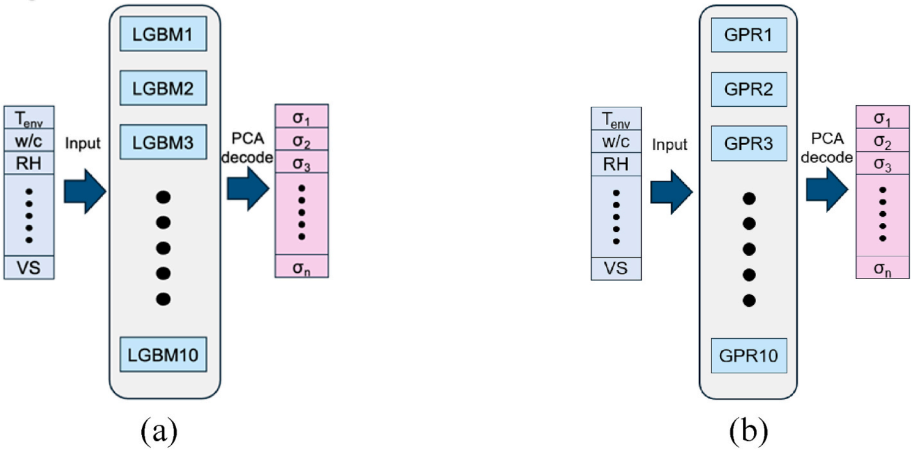

(a)

(b)

Fig. 9. Point-wise prediction models for EAS prediction: (a) LGBM models; (b) GPR models.

optimized hyperparameters include the number of estimators, maximum depth, learning rate, number of leaves, minimum child samples, subsampling ratio, feature subsampling ratio, and L1/L2 regularization terms.

For GPR, a separate regressor is likewise trained for each retained PC using a kernel composed of a constant term, an RBF kernel, and a white-noise term. The kernel hyperparameters are optimized automatically during model fitting through log-marginal-likelihood maximization, with three optimizer restarts for improved robustness. The testing results of these point-wise models are then compared with those of the sequence model in Section 4.3.

3.2.2. *Sequence prediction models*

EAS exhibits local correlations and path dependence. Point-wise models assume independence across points and therefore might neglect the underlying dynamics. Sequence models, by conditioning each step on prior history, potentially can address this limitation. In this study we adopt a Gated Recurrent Unit (GRU) to model history dependence in the EAS trajectory. Compared with vanilla RNNs, GRUs introduce gating mechanisms that regulate the contribution of past hidden states, mitigating vanishing gradients. Compared with LSTM, GRU has a simpler architecture with fewer trainable parameters and lower computational cost, which makes it attractive for the present problem involving a moderate sample size and repeated model updates in the active-learning framework. Therefore, GRU was adopted here as an efficient sequence model that offers a favourable effectiveness–cost trade-off (Chung et al., 2014). Given an input sequence X_t and hidden state H_{t-1}, a GRU updates its state using two gates, the reset gate R_t and the update gate Z_t:

$$R_t = \sigma(X_t W_{xr} + H_{t-1} W_{hr} + b_r) \tag{14a}$$

$$Z_t = \sigma(X_t W_{xz} + H_{t-1} W_{hz} + b_z) \tag{14b}$$

where W, b are the weights and biases of the corresponding fully connected networks that transforms for inputs and states (e.g., W_{xr} maps X_t to the reset gate; W_{hr} maps H_{t-1} to the reset gate). The candidate hidden state $\widetilde{H_t}$ can then be obtained by integrating the previous state with the reset gate:

$$\widetilde{H_t} = \tan h(X_t W_{xh} + (R_t \odot H_{t-1}) W_{hh} + b_h) \tag{14c}$$

where tanh is the activation function and $\odot$ is the elementwise product operator. Finally, the new hidden state H_t is a combination of the previous and candidate state:

$$H_t = Z_t \odot H_{t-1} + (1 - Z_t) \odot \widetilde{H_t} \tag{14d}$$

Therefore, the reset gate R_t controls how much past information is exposed when forming candidate state $\widetilde{H_t}$, while the Z_t controls how much of $\widetilde{H_t}$ replaces the old state.

The proposed GRU-based network architecture is shown in Fig. 10. The network has a two-branch input. The static branch takes material design variables, environmental conditions, and geometry (Table 1) and maps them with a ReLU MLP to a fixed static embedding f. The temporal branch takes the time index sequence $t = 1, 2, 3, \ldots, 672$ and produces dynamic embeddings v_n $(n = 1 \sim 672)$, each obtained by a ReLU MLP. Both branches are linearly projected to the same width and fused by element-wise addition $f + v_n$, so that each step receives identical static context plus its own temporal code. The fused sequence is processed by a stack of three GRU layers to produce hidden states k_n $(n = 1 \sim 672)$. An attention pooling module is used to extract the time-dependent information from k_n and aggregates it further into a 128×1 vector which is fed into a MLP with Monte Carlo Dropout (MCD) to predict the 10×1 PCs. Finally, the PCs can be inversely transformed to obtain the 672×1 EAS vector. The training minimizes a composite loss over the PC space and stress space:

$$L = \lambda_{PC} MSE_{PC} + \lambda_{\sigma} MSE_{\sigma} \tag{15}$$

where $\lambda_{PC} = 0.1$ and $\lambda_{\sigma} = 0.9$ weight the PCA-space and stress-space MSE terms, respectively.

In this network architecture, the MCD is applied at the MLP head after the GRU layers. A dropout rate of 0.3 was adopted in the MC Dropout head, as a brief parametric study (Appendix A) showed that this value preserves near-optimal predictive accuracy while providing improved uncertainty coverage. Following the Bayesian view, keeping dropout active at inference yields a stochastic ensemble whose variability approximates the posterior predictive (Gal and Ghahramani, 2016). Therefore, during the inference, the Monte-Carlo analysis can be applied for quantifying the uncertainty. In this paper, 100 stochastic forward passes are performed for each input sample to obtain the predictive mean and variance.

The GRU–MCD model is first trained on the LHS dataset—using the same 70/15/15 train/validation/test split as the point-wise baselines—to enable a fair comparison. Although GRU–MCD provides predictive uncertainty that could, in principle, drive active learning (AL), its uncertainty estimates are sample-size sensitive and can be unreliable in the early AL iterations. Therefore, we pair GRU–MCD with a Gaussian Process (GP) in an AL setting and retrain on the AL dataset to assess the benefit of uncertainty-based sampling. All training uses a learning rate of 10^{-4}, batch size 32, and up to 400 epochs, with early stopping based on validation loss (patience 20 epochs).

4. Results and discussion

4.1. TCM modelling results

4.1.1. Qualitative results

This section presents a qualitative analysis of the TCM model. First, the results of the TCM model on a specific parameter setting at 24 h (Table 4) is shown in Fig. 11. The case study reveals general patterns of the temperature and EAS. To quantify such process, the evolution of temperature and EAS is calculated by averaging the results of all the Gaussian points at the middle section of the wall (i.e., section B-B in Fig. 7). Since concrete is usually very sensitive to tensile cracking, the first principal stress is often used to characterize its cracking risk. In this scenario, instead, the longitudinal stress component is used because 1) it closely aligns with the first principal stress during shrinkage when tensile stress dominates; and 2) it retains the initial expansion-induced compressive stress which is also important for EAC risk analysis.

The cement hydration reaction releases heat that results in temperature increase in the wall. Then, heat exchange with the ambient environment drives cooling, producing a core-to-edge temperature gradient (Fig. 11(a–b)). Meanwhile, the associated thermal deformation, together with autogenous and drying deformations due to hydration and moisture transport, is restrained by the hardened base, leading to the development of EAS. The longitudinal stress first becomes compressive when early expansion is restrained and later turns tensile during the shrinkage-dominated period (Fig. 11(c–d)). The restraint is strongest at the wall–base interface near the mid-span; consequently, the longitudinal stress field is largest there and decays progressively from the bottom of the mid-section toward the free edges of the wall. If the EAS at some point exceeds the tensile strength, EAC happens. EAS is crucial for the EAC analysis and therefore it is the main target of the ML modelling.

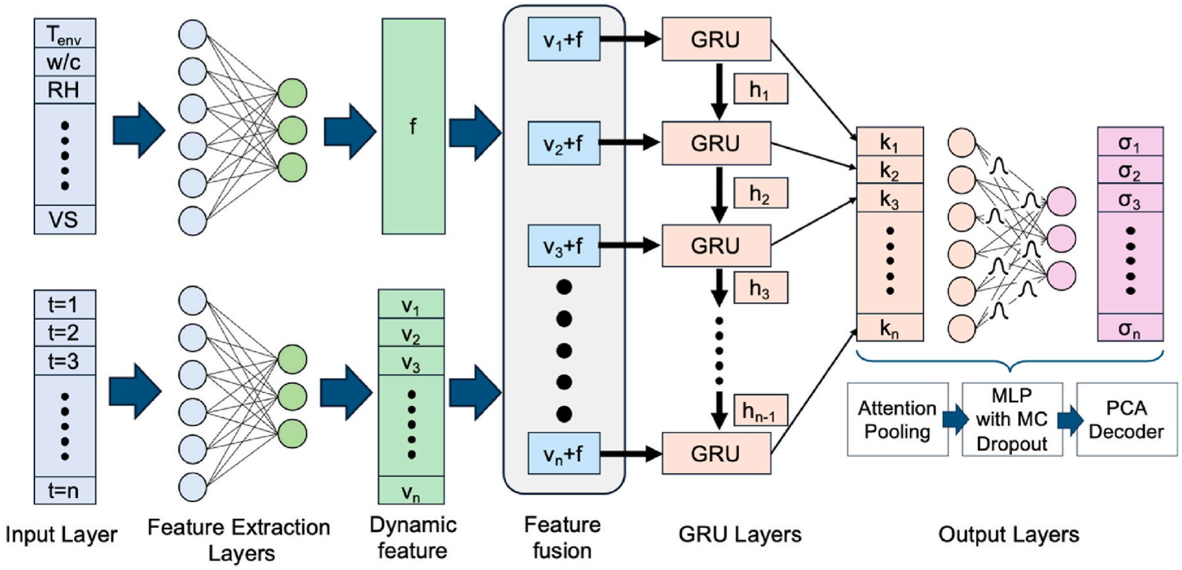

Fig. 10. The GRU-MCD architecture for EAS prediction.

Table 4
Parameters for the qualitative study.

T_room	RH	len	width	height	tc	cem	wc	agg	agg_type	cem_ type	b_h_ratio	*E_b_ ratio*	VS
25.14	0.78	10.59	0.32	4.04	37.60	303.13	0.49	6.04	2	1	0.28	1.94	144.24

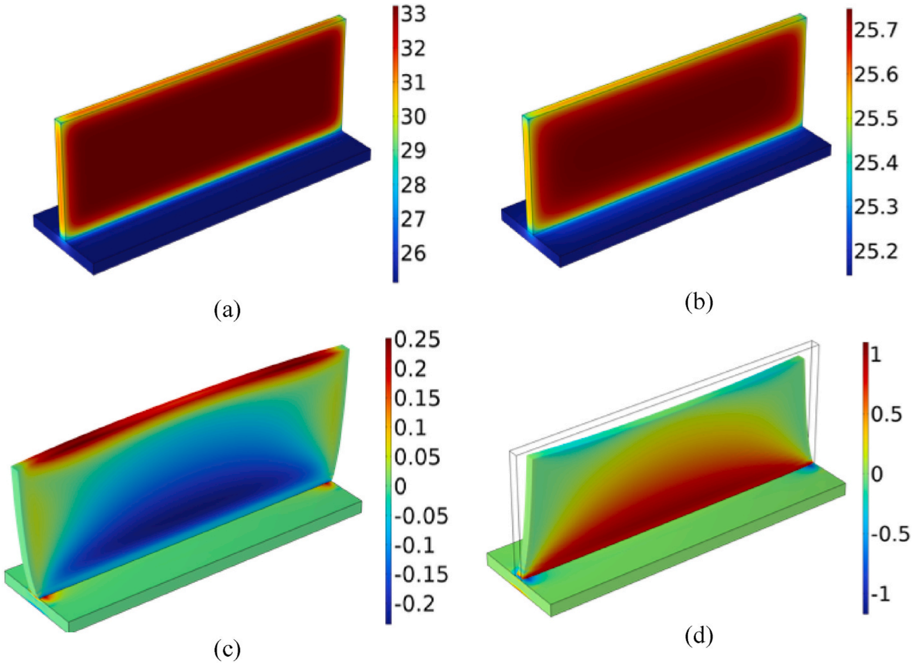

(a) (b) (c) (d)

Fig. 11. Results of the case study: (ã b) Temperature at 24h and 168h respectively (units: °C); (c ~ d) Longitudinal stress at 24h and 168h respectively (units: MPa). Note that 24h corresponds to the heating/expansion phase, whereas 168h corresponds to the cooling/shrinkage phase.

4.1.2. *Experimental verification*

This section aims to compare the TCM modelling results and experimental observations. Specifically, because the thermo-fields and chemo-fields have been systematically calibrated and validated in literatures such as (Di Luzio and Cusatis, 2009b), this section focuses on validation of the mechanical field, which involves Eqs. 8–13. Such validation has been challenging since it involves several critical time-dependent behaviors/properties, including creep, shrinkage, and elastic modulus as the input and the EAS as the output.

TSTM is one of the few testing methods that can measure all these behaviors/properties almost at the same time, but such tests are too expensive and therefore only a few tests can be performed to (partially) validate the model. For example, Liang et al. used the Volterra integral (Eq. (8)) and exponential algorithm to simulate the EAS evolution of various concretes (e.g., ordinary Portland cement concrete, high-volume slag concrete and alkali-activated slag concrete), which was validated by conventional TSTM tests (Liang et al., 2022b, 2023b; Li et al., 2022). In these tests, the deformation, stress, and elastic modulus were obtained from experiments, but the creep compliance function was reversely calculated or assumed and therefore provides only "partial" validation of the mechanical field. In addition, based on the conventional TSTM tests on alkali activated slag concrete, the creep compliance function was tested and converted to relaxation modulus using the exponential conversion (Eq. (10)). Using the mid-point rule, the Volterra integral was discretized and therefore the EAS was calculated, which well matched the experimental results (Li et al., 2025).

Based on the Mini-TSTM, which enhances the testing efficiency, a more comprehensive validation of the mechanical fields was possible. In (Liang et al., 2024b, 2024c, 2024d), the Liang et al. conducted Mini-TSTM tests on concrete and cement pastes with different binders and water cement ratios under different temperature conditions. The deformation, elastic modulus, and creep were tested, and these data were used as the input of a viscoelastic model based on Eq. 8–13 to predict the EAS, which was compared with the experimental results and showed good accuracy. Some of these comparison results are shown in Fig. 12. The validation involves two different cements, ordinary Portland Cement (i.e., CEM I 42.5N) and high-volume slag cement (i.e., CEM III/B 42.5N, with slag mass volume around 70%), under temperatures ranging from 10 to 40 °C. Both cements correspond to *cement_type* = 2 in Table 2. The consistency between the experiment and simulation validates the applicability of the proposed viscoelastic model in the TCM framework for a general analysis of EAC risks under different temperatures. For more details the readers are to referred to (Liang et al., 2024b, 2024c, 2024d).

4.2. *Database overview*

This section presents the overview of database constructed by the TCM model. Using the LHS sampling, 1000 sample points are generated to cover the parameter ranges as in Table 1. The distribution of the LHS sampling database is shown in Fig. 13. Note that the samples using low w/c ratios and high strength cement (i.e., cem_type = 3) are removed from the database as such combination is very rarely used in practice.

Using the TCM model, the EAS curve of each sample shown in Fig. 14 can be obtained and then characterized by PCA using the Scikit-Learn library (Pedregosa et al., 2012). The PCA results indicate that the first few components can capture most of the variance of the original 672×1 EAS curve, as shown by the explained variance in Fig. 14(a). In particular, although the first PC alone accounts for more than 95% of the explained variance, it is not sufficient to reconstruct the EAS curve accurately, and some local shape features may still be lost. Through repeated reconstruction trials, it was found that retaining 10 PCs

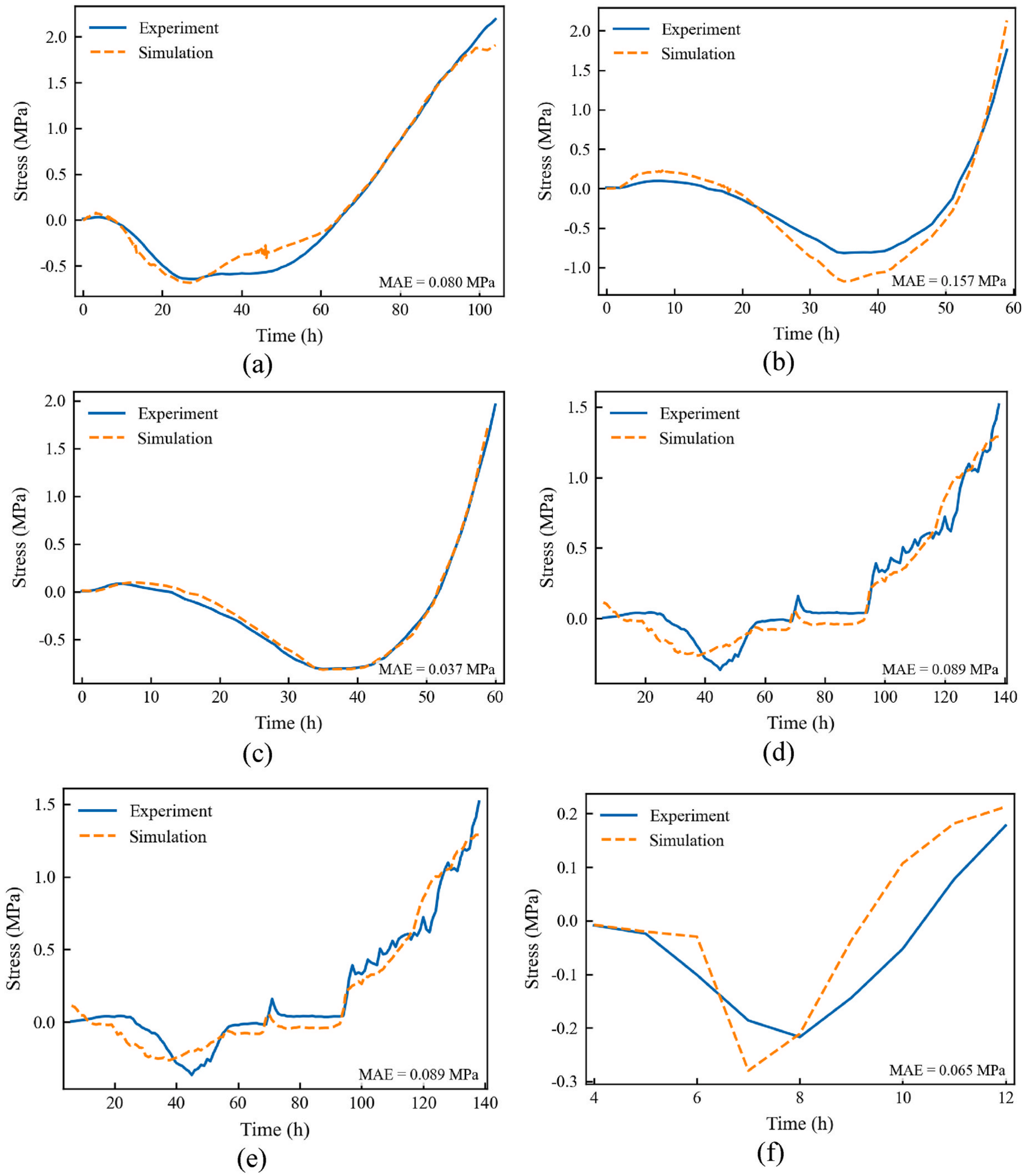

Fig. 12. Comparison of the predicted and tested EAS: (a) CEM I 42.5N, w/c = 0.30 tested under 20 °C; (b-c) Two different batches of CEM III B 42.5N, w/c = 0.30 tested under 20 °C; (d-f) CEM I 42.5N, w/c = 0.30 tested under 10 °C, 30 °C, and 40 °C respectively (Liang et al., 2024b, 2024c, 2024d).

provides a good balance between dimensionality reduction and reconstruction fidelity, especially for preserving finer details of the curve. Therefore, the first 10 PCs were adopted in this study, and the comparison between the reconstructed and original EAS curves is shown in Fig. 14(b).

The first PC corresponds to over 95% of the explained variance. Since the PCA is essentially not an explainable model, parametric study as shown in Fig. 15 is conducted to analyze its statistical characteristics and understand its physical representations. By ramping the first and second PC from the minimum (i.e., −29.22 and −16.32) to the maximum (i.e., 78.18 and 16.38), the EAS curves with similar shapes while different EAS magnitudes and directions can be obtained. Some patterns can already be found: 1) Larger 1st PC results in EAS curves with the same shape and direction (i.e., initially in compression and later tension) and larger EAS magnitudes. 2) The 2nd PC is negatively correlated to the EAS. Therefore, larger 1st PC means higher stress and more EAC risk, and vice versa for the 2nd PC.

Bearing the representation pattern of 1st and 2nd PC in mind, the correlation map between the input parameters and the PCs can be analyzed, as shown in Fig. 16. Some distinct patterns can already be found from the correlation maps. For example, the first three parameters that are clearly positively correlated to 1st PCs are the ambient temperature (*T_room*), length of the wall (*len*), and cement amount (*cem*), which aligns with the common understanding of thermal cracking in massive concrete (Fairbairn and Azenha, 2019; Xin et al., 2021): 1) The temperature accelerates both the deformation rate and the evolution of

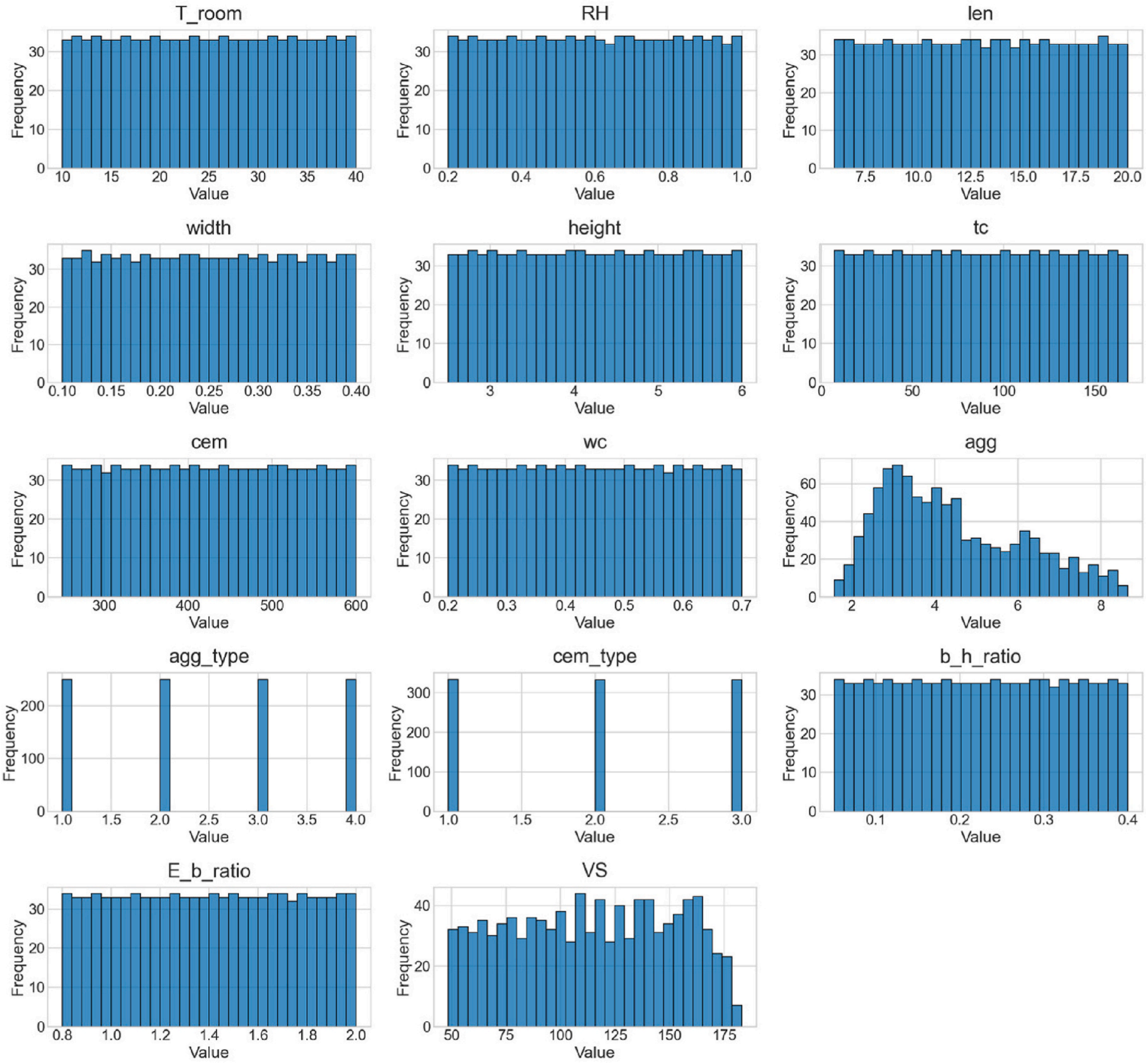

Fig. 13. Histogram of the database generated by LHS sampling.

mechanical properties, resulting in rapid increase of the EAS (Liang et al., 2024d); 2) Increasing the length of the wall and the amount of cement both contributes to the total heat released in the hardening, therefore causing the increase of temperature and EAS subsequently; 3) Increasing the wall length also results in stronger restraining effects in the middle span of the wall and therefore results in the EAS increase. It should be noted that the wall thickness also positively correlates with the overall stress level, which are only reflected through its negative correlation with the 2 nd PCs, indicating a less dominating role. Such minor effects may be due to the current parameter range of the wall thickness (0.1–0.4 m), which corresponds to typical residential concrete structures. In contrast, early-age cracking risks become much more pronounced in truly massive concrete elements, where thicknesses commonly reach 0.7 m or more (Jędrzejewska et al., 2020).

4.3. *Modelling performance*

This section presents the performance of the point-wise ML models trained using the LHS sampling data, as shown in Fig. 17, and the sequential model Gated Recurrent Unit with Monte Carlo Dropout (GRU-MCD), shown in Fig. 18. The mean squared error (MSE) and coefficient of determination (R^2), calculated using the standardized data, are summarized in Table 5. In general, all models can reproduce the EAS reasonably well, with most prediction points distributed close to the 1:1 line and relatively high R^2 values on the validation and testing sets. For GPR, the almost perfect fit on the training set ($R^2 = 0.999$) together with the visibly larger scatter on the validation and testing sets ($R^2 = 0.922$ and 0.913, respectively) indicates a noticeable tendency toward overfitting (Fig. 16(a–c), Table 5). LGBM exhibits a similar pattern, with $R^2 = 0.992$, 0.903, and 0.905 on the training, validation, and testing sets, respectively, and slightly larger validation and testing errors than GPR, indicating comparatively weaker generalization performance (Fig. 16 (d–f), Table 5).

In contrast, GRU-MCD shows a much smaller gap between the training, validation, and testing results, with $R^2 = 0.984$, 0.957, and 0.952, respectively, and also achieves the lowest validation and testing MSE values among all three models (Table 5). As shown in Fig. 18, the prediction points of GRU-MCD remain more tightly clustered around the 1:1 line for both the validation and testing sets, indicating more robust generalization. This improvement can be attributed to the sequential GRU architecture, which is better suited to capturing the temporal dependencies in the evolving stress histories, together with the regularization effect introduced by Monte Carlo dropout during training. Moreover, the GRU-based framework provides a natural basis for incorporating future time-dependent input features, making it particularly suitable for general early-age stress prediction problems.

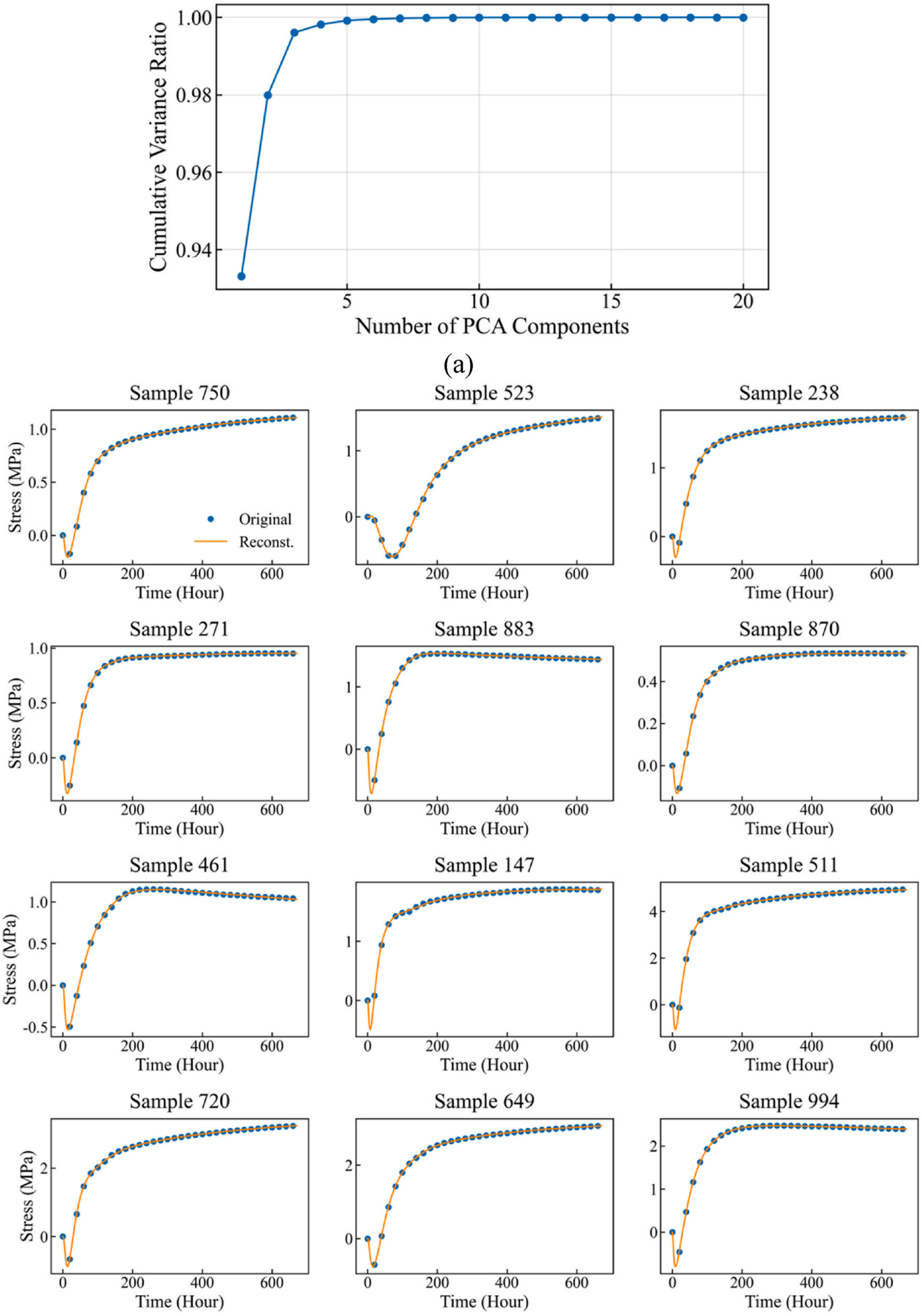

(b)

Fig. 14. PCA results: (a) explained variance and (b) comparison of original EAS and the reconstructed EAS using PCA.

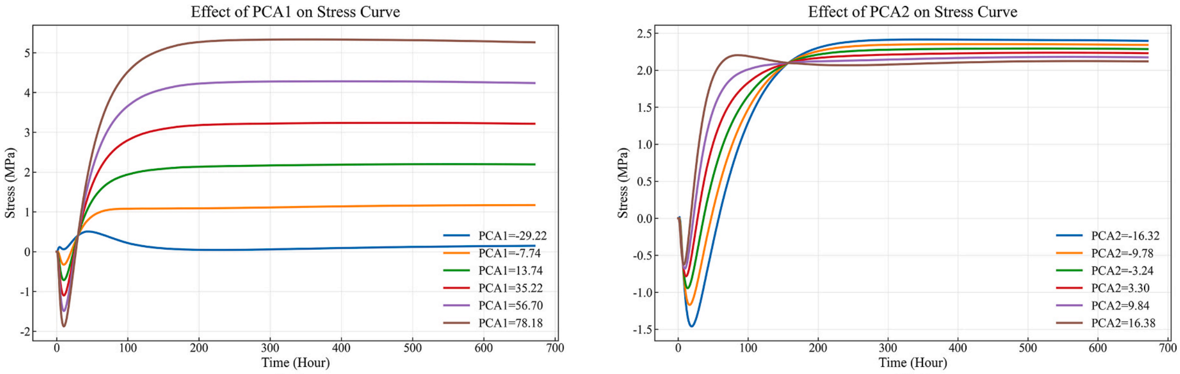

(a) (b)

Fig. 15. Parametric study of the first (a) and second (b) PCs.

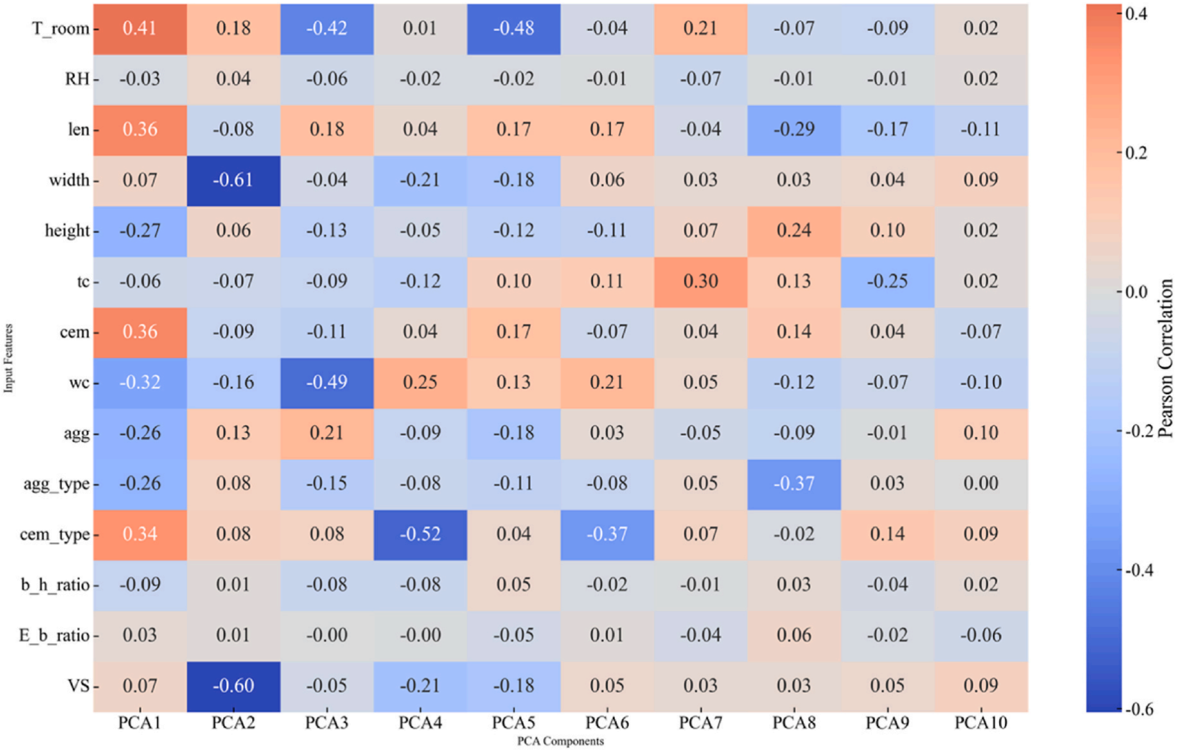

	PCA1	PCA2	PCA3	PCA4	PCA5	PCA6	PCA7	PCA8	PCA9	PCA10
T_room	0.41	0.18	-0.42	0.01	-0.48	-0.04	0.21	-0.07	-0.09	0.02
RH	-0.03	0.04	-0.06	-0.02	-0.02	-0.01	-0.07	-0.01	-0.01	0.02
len	0.36	-0.08	0.18	0.04	0.17	0.17	-0.04	-0.29	-0.17	-0.11
width	0.07	-0.61	-0.04	-0.21	-0.18	0.06	0.03	0.03	0.04	0.09
height	-0.27	0.06	-0.13	-0.05	-0.12	-0.11	0.07	0.24	0.10	0.02
tc	-0.06	-0.07	-0.09	-0.12	0.10	0.11	0.30	0.13	-0.25	0.02
cem	0.36	-0.09	-0.11	0.04	0.17	-0.07	0.04	0.14	0.04	-0.07
wc	-0.32	-0.16	-0.49	0.25	0.13	0.21	0.05	-0.12	-0.07	-0.10
agg	-0.26	0.13	0.21	-0.09	-0.18	0.03	-0.05	-0.09	-0.01	0.10
agg_type	-0.26	0.08	-0.15	-0.08	-0.11	-0.08	0.05	-0.37	0.03	0.00
cem_type	0.34	0.08	0.08	-0.52	0.04	-0.37	0.07	-0.02	0.14	0.09
b_h_ratio	-0.09	0.01	-0.08	-0.08	0.05	-0.02	-0.01	0.03	-0.04	0.02
E_b_ratio	0.03	0.01	-0.00	-0.00	-0.05	0.01	-0.04	0.06	-0.02	-0.06
VS	0.07	-0.60	-0.05	-0.21	-0.18	0.05	0.03	0.03	0.05	0.09

Fig. 16. Correlation map between the input parameters and PCs.

4.4. GP-guided active learning

The GRU-MCD model is trained using data sampling techniques of LHS and AL. Starting with an identical initial dataset consisting of 64 randomly selected samples, additional data points were progressively incorporated from LHS and AL to construct two separate models. Their predictive performance was then cross-evaluated: the LHS-based model was tested on the AL dataset, while the AL-based model was tested on the LHS dataset. The modelling performance is shown in Fig. 19.

As expected, both models exhibit monotonic performance improvements as the number of training samples increases, as quantified by MSE and R^2 in Fig. 19(a and b). The most substantial improvements occur within the first 300 samples. Notably, the model trained with AL data consistently outperforms the LHS-based model across most training stages. From the MSE curves, it is particularly evident that the AL-based model trained with only ~200 samples already achieve prediction accuracy comparable to the LHS-based model trained with ~900 samples, highlighting the significant efficiency benefits brought by AL. Such performance gain can be attributed to the uncertainty-guided sample selection strategy employed in AL. At each acquisition step, the variance estimated by the GP model is used as the acquisition score to identify the most informative samples. As AL progresses, the distribution of acquisition scores gradually shifts from high to low variance (Fig. 19(c)), indicating a continuous reduction in uncertainty across the sampling space. This trend is most prominent within the first 300 acquisition cycles, corresponding well to the rapid improvement observed in model performance.

This efficiency advantage is practically important from a computational perspective. In the present study, the dominant computational cost lies in generating labeled samples with the TCM model rather than in training the DSL surrogate. Specifically, each TCM simulation requires approximately 0.7–1.0 h per sample on an Intel i9-14900K CPU with 64 GB RAM, whereas training the DSL model for 400 epochs with 1000 samples takes only about 5 min on an NVIDIA RTX 3060 GPU. Therefore, reducing the number of required TCM samples can directly translate into substantial savings in the total wall-clock time.

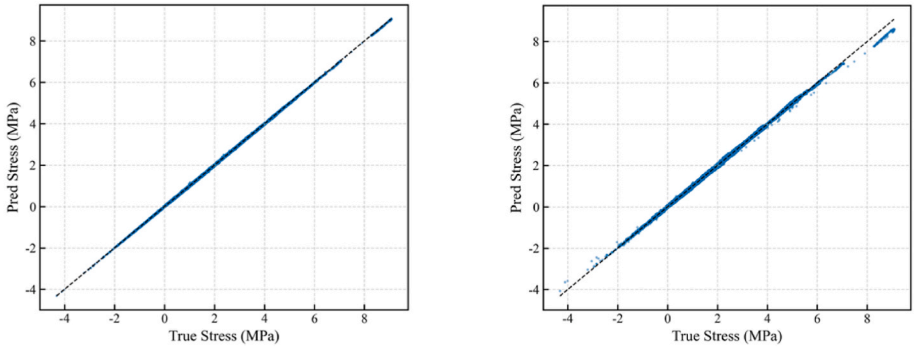

(a) GPR training

(d) LGBM training

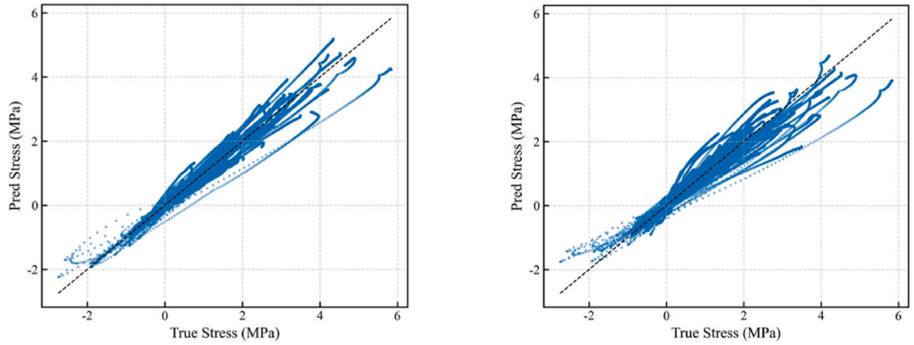

(b) GPR validation

(e) LGBM validation

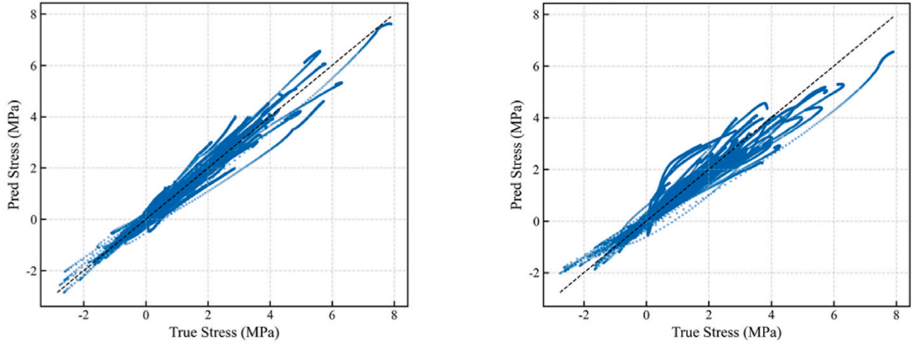

(c) GPR testing

(f) LGBM validation

Fig. 17. Performance of the point-wise machine learning models: (ã c) are the results of GPR models and (c ∼ d) are the results of LGBM models over the training, validation and testing set respectively.

Overall, the AL procedure effectively targets the most uncertain regions of the input space, resulting in a rapid contraction of predictive uncertainty. This targeted sampling strategy leads to a far more efficient training process and produces a model with superior generalization performance compared to conventional LHS-based data sampling.

4.5. *Case study*

This section presents a case study investigating the influence of key material and structural parameters on the evolution of early-age stress. A representative sample is randomly selected as the baseline, with its parameter values listed in Table 6. Using this baseline, the effects of temperature, wall length, wall height, and cement content on EAS evolution are illustrated in Fig. 20, where the curves shown correspond to the EAS mean and the bands representing twice the standard deviation.

The observed trends are consistent with the correlation patterns identified in the database analysis (Section 4.2) and align well with established mechanistic understanding of early-age concrete behavior. As shown in Fig. 20(a), increasing temperature accelerates cement hydration, which intensifies both thermal and autogenous deformation and ultimately leads to higher EAS. A similar pattern is observed for cement content (Fig. 20(b)): higher cement amounts generate more hydration heat, thereby increasing thermal deformation and elevating EAS. The geometric parameters—wall length and height—reflect the level of structural restraint. A longer wall exhibits a greater degree of restraint, resulting in higher stress development, whereas an increase in height reduces restraint and consequently lowers EAS (Fig. 20(c and d)). This observation is consistent with the well-established understanding that the length-to-width ratio is a critical determinant of EAC risk: structures with a higher length-to-width ratio generally experience more severe restraint effects and are therefore more susceptible to elevated EAS and EAC (Jędrzejewska et al., 2020).

Beyond capturing these physically meaningful trends, the proposed modeling framework provides not only point predictions but also 95% confidence intervals. This uncertainty indication is particularly valuable for engineering design and structural reliability assessment, enabling more informed and risk-aware decision-making.

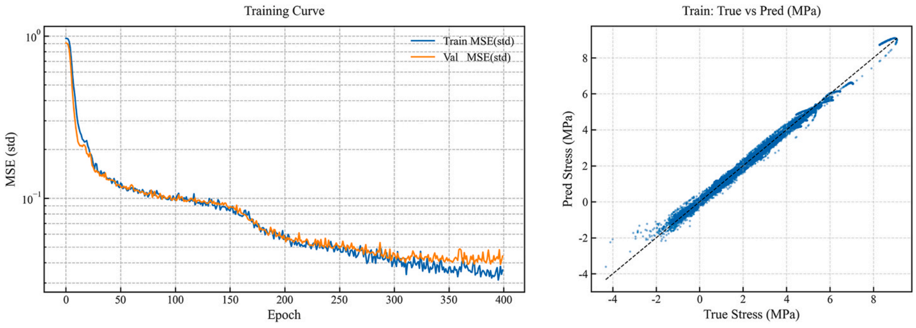

(a) Loss history (b) GRU-MCD Training

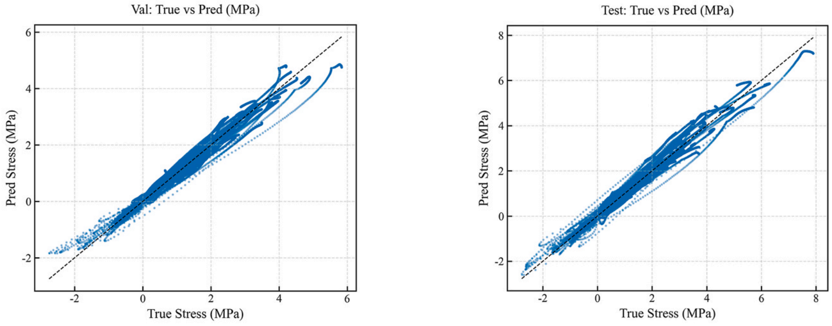

(c) GRU-MCD Validation (d) GRU-MCD Testing

Fig. 18. Performance of the sequential model GRU-MCD: (a) training loss history and (b ∼ d) the results of over the training, validation and testing set respectively.

Table 5
Metrics of the model performance.

	Training		Validation		Testing	
	MSE	R^2	MSE	R^2	MSE	R^2
GP	**0.001**	**0.999**	0.089	0.922	0.092	0.913
LGBM	0.008	0.992	0.131	0.903	0.163	0.905
GRU-MCD	0.015	0.984	**0.039**	**0.957**	**0.058**	**0.952**

4.6. Discussion

Overall, the present study demonstrates that EAS prediction can be improved from both the physical and data-driven perspectives. The proposed TCM model provides a physically grounded basis for EAS simulation and shows good agreement with experimental observations, while the GRU-MCD sequence model is better suited than point-wise predictors for capturing the path-dependent evolution of the full EAS curve. More importantly, the GP-guided AL strategy substantially improves data efficiency, enabling high predictive accuracy with far fewer expensive TCM samples. These results suggest that the overall FE-ML-AL workflow is transferable and can be extended to other material systems and structural scenarios.

At the same time, several limitations remain. On the material side, the current model is still mainly based on the MC2010 framework, and although some components have been improved using XGBoost, the prediction accuracy of complex time-dependent behaviours still requires further refinement. In particular, the present framework uses equivalent age as a unified index to describe the evolution of several material properties. While such a treatment is relatively reasonable for strength development and creep/relaxation, its applicability to shrinkage, especially autogenous shrinkage, is less rigorous (Liang et al., 2024d). This is because shrinkage is more directly governed by moisture-related mechanisms and self-desiccation and may not strictly follow the same maturity scaling as strength-related properties. In addition, the chemical field in the current material model only considers the hydration of ordinary Portland cement. The influences of chemical admixtures and other cementitious materials with different hydration kinetics are not explicitly included. The hydration degree is currently determined by an Arrhenius-type ordinary differential equation, which remains essentially empirical. As a result, the current material module still involves simplified assumptions in both the treatment of different time-dependent behaviors and the chemo-field evolution, which should be refined in future developments.

On the structural side, the present mechanical idealization is relatively simplified, whereas real structures may involve more complex structural forms, restraint conditions, foundation effects, and construction sequences. These factors should be considered more carefully in future developments. In particular, the present model involves assumptions on the construction and curing process. For example, the curing condition is simplified as blanket covering, whereas actual engineering practice may involve other curing measures, together with environmental effects such as solar radiation and wind-induced cooling. These factors mainly affect the parameter setting of the thermos-field and may further influence the subsequent stress evolution. In addition, the geometric idealization is simplified, and the interaction with surrounding or adjacent structural components is not explicitly considered. This is directly related to the definition of restraint conditions, which is particularly important for EAS calculation. Furthermore, the environmental temperature considered in this study is limited to 10–40 °C, which covers most common residential exposure conditions. Extending the model to a wider temperature range is not difficult from an implementation point of view, since both the physical model and the neural-network framework can accommodate variable temperature histories. However, such an extension should be supported by corresponding material models, because the applicability of the current MC2010-based formulation outside this temperature range remains unclear.

In addition, although Monte Carlo dropout provides a useful estimate of predictive uncertainty, the current results mainly support uncertainty indication rather than fully calibrated uncertainty quantification. As shown in Appendix A, increasing the dropout rate improves uncertainty coverage but also reduces point-prediction accuracy, so the adopted setting is a compromise between these two objectives. The resulting

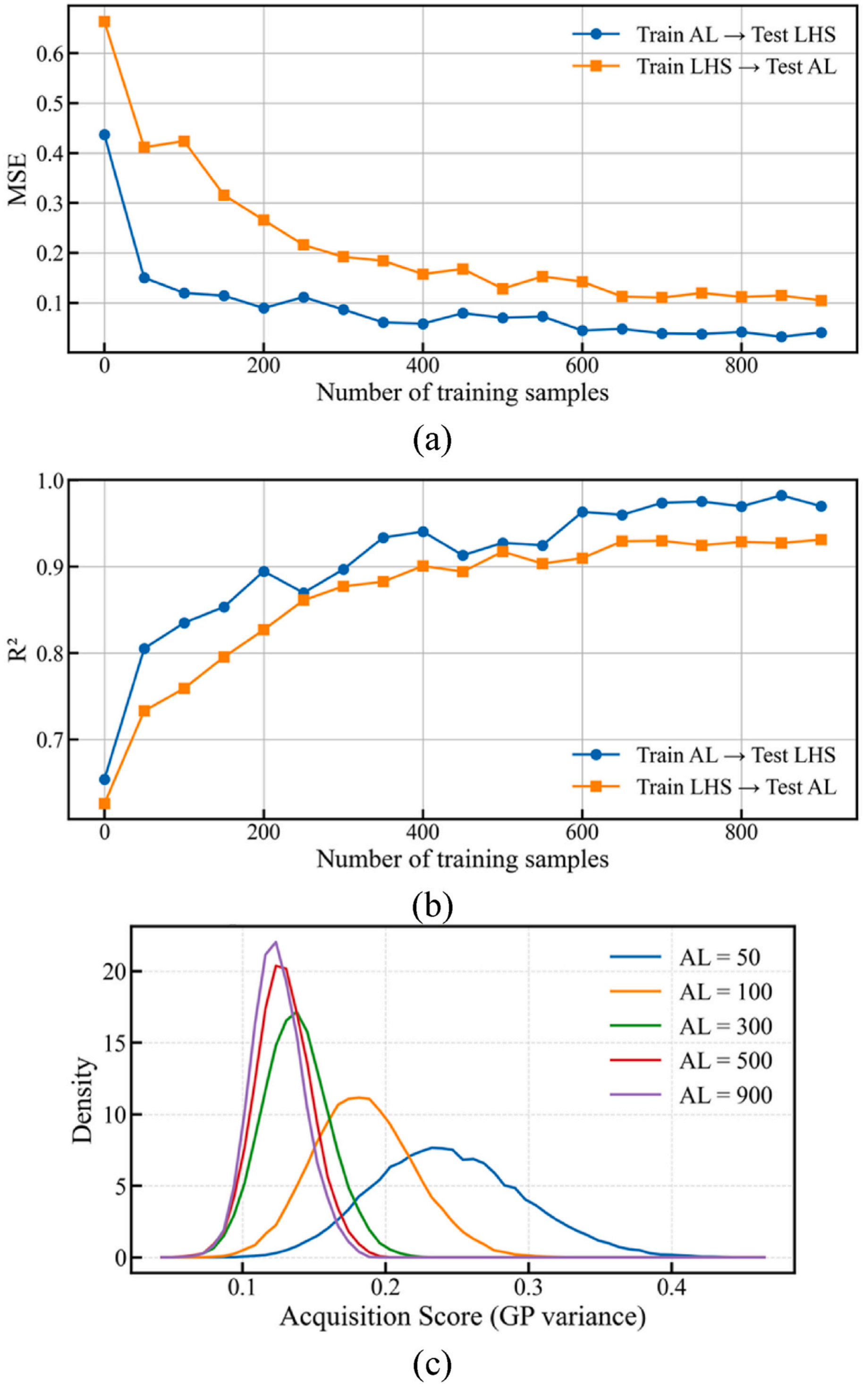

Fig. 19. Performance of the GRU-MCD trained by different sampling techniques and sample numbers: (a) MSE (b) R^2 and (c) the probability density of acquisition score in AL process given different sample numbers.

Table 6
Parameters for the case study.

T_room	RH	len	width	height	tc	cem	wc	agg	agg_type	cem_ type	b_h_ratio	*E_b_ ratio*	VS
21.72	0.87	19.01	0.17	3.04	58.72	502.74	0.45	3.23	2	1	0.17	1.78	82.72

empirical coverage still remains below the nominal 95% confidence level, indicating that the uncertainty intervals are not yet fully calibrated. This limitation is consistent with recent studies showing that uncertainty estimates from Monte Carlo dropout can depend strongly on

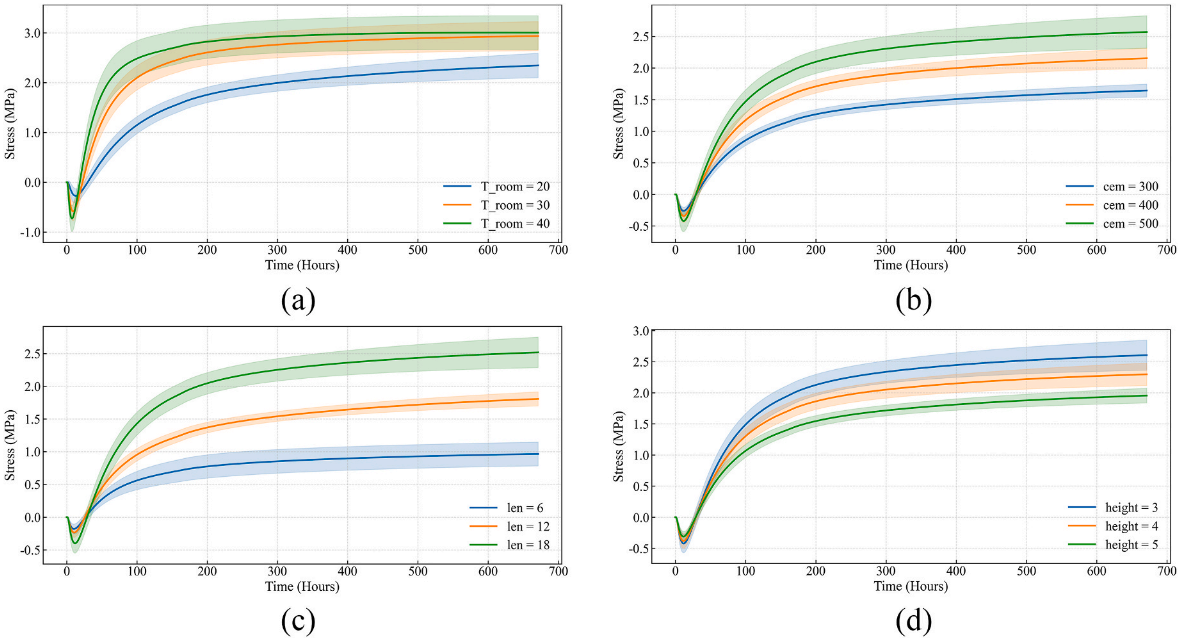

Fig. 20. Parametric study of the GRU-MCD trained on the AL dataset:
(a) temperature; (b) cement amount; (c) length; (d) height. (The shaded area represents 95% confidence intervals).

the model design and may be difficult to interpret in a rigorous probabilistic sense (Pasparakis et al., 2025).

Future work may therefore proceed along four directions. First, more experimental data are needed to support improved modelling of time-dependent material behaviors under complex environmental conditions, especially creep, autogenous shrinkage, and drying shrinkage. The material model itself should be further improved by incorporating admixture effects, other cementitious systems, and more physically based descriptions of hydration kinetics beyond the current Arrhenius-type empirical formulation. Second, a more flexible and powerful structural modelling module should be developed to account for more complicated structural forms, restraint conditions, construction processes, adjacent structural interactions, and wider environmental temperature histories. Third, uncertainty calibration should be examined more systematically by introducing explicit quantitative evaluation measures and by exploring more robust probabilistic learning strategies beyond Monte Carlo dropout (Pasparakis et al., 2025). Fourth, more advanced data- and physics-driven extensions may also be explored, including emerging neural architectures such as Kolmogorov-Arnold networks (Wang et al., 2025), operator-learning (Xu et al., 2024), physics-informed neural networks (Shen et al., 2025; Wang et al., 2026), and the integration of machine learning with multi-objective optimization for structural design (Zhang et al., 2026b).

5. Conclusions

This study presents a unified framework for predicting the EAS evolution of cementitious materials by integrating TCM modelling, DSL, and uncertainty-driven AL. A TCM model with experimentally informed viscoelasticity was developed to generate high-fidelity stress–time datasets across diverse material compositions, environmental conditions, and structural configurations. These datasets were used to train a GRU-based DSL model capable of learning the full EAS evolution history. To reduce the computational burden of multifield simulations, a GP-guided DSL strategy was introduced, enabling efficient sample selection and fast model refinement. Together, this FE–ML framework significantly improves both the accuracy and efficiency of EAS prediction. The main findings are as follows:

1) An enhanced TCM model was established using a 9-unit Maxwell chain derived from an exponential creep–relaxation conversion and solved by the exponential algorithm in FEM. This formulation guarantees positive relaxation modulus and numerical efficiency, avoiding the drawbacks of direct Volterra inversion. The complete viscoelastic model—covering creep, shrinkage, and stiffness development—was validated against extensive Mini-TSTM tests under varying temperatures and binder types. It accurately reproduced the observed EAS evolution, demonstrating strong reliability for EAC assessment.
2) Compared with point-wise models such as LGBM and GPR, the GRU-MCD sequence model captured the temporal dependency of EAS evolution much more effectively. It achieved the highest accuracy ($R^2 > 0.95$), with reduced overfitting. Its ability to combine time-series information, structural and material parameters, and predictive uncertainty makes it well suited for modelling path-dependent early-age mechanical behavior of cementitious materials.
3) The GP-guided AL scheme greatly improved data efficiency by prioritizing the most informative samples. Using only ~200 AL-selected simulations, the GRU-MCD model reached or exceeded the accuracy (in terms of MSE) of models trained on ~900 LHS samples. The steady decrease in acquisition variance confirmed that AL efficiently targets high-uncertainty regions, accelerates surrogate-model convergence, and reduces reliance on computationally expensive TCM analyses.

Although the present study employed a specific wall–base structure and an AI-enhanced MC2010-based material model as an example, the proposed FE–ML framework shows good potential for extension to other structural configurations, geometries, and cementitious systems, provided that the corresponding temperature, hydration, and viscoelastic properties can be properly defined. At the same time, the present material and structural models still involve several simplifying assumptions, including the treatment of hydration kinetics, shrinkage evolution, curing conditions, restraint definition, and environmental temperature range. In addition, although the GRU-MCD model can predict full stress evolution curves and provide useful uncertainty estimates through Monte Carlo dropout, the current uncertainty output is more suitable for uncertainty indication than for fully calibrated probabilistic assessment. Therefore, future work should focus on improving the material model, refining the structural representation, and strengthening uncertainty calibration, so as to further enhance the applicability of the proposed framework to reliability-oriented analysis, risk-informed design, and optimization of low-carbon concrete mixtures and structural configurations in early-age performance assessment.

CRediT authorship contribution statement

Minfei Liang: Writing – original draft, Validation, Software, Methodology, Investigation, Formal analysis, Data curation, Conceptualization. **Yong Fang:** Writing – review & editing, Funding acquisition, Formal analysis. **Wenqi Guo:** Writing – review & editing, Investigation, Conceptualization. **Chuan He:** Writing – review & editing, Investigation, Funding acquisition, Conceptualization. **Erik Schlangen:** Writing – review & editing, Investigation, Formal analysis, Conceptualization. **Branko Šavija:** Writing – review & editing, Investigation, Formal analysis, Conceptualization. **Sonia Contera:** Writing – review & editing, Funding acquisition, Formal analysis, Conceptualization.

Declaration of competing interest

The authors declare that they have no known competing financial interests or personal relationships that could have appeared to influence the work reported in this paper.

Appendix. A Sensitivity analysis of dropout rate

To justify the choice of the dropout rate in the MC Dropout procedure, a brief parametric study was conducted by varying the dropout rate from 0.1 to 0.5. For each setting, the GRU-MCD model was trained under the same configuration, and the predictive performance on the test set was evaluated in terms of R^2, MSE, and uncertainty coverage. The results are summarized in Fig. A1.

Herein, the uncertainty coverage is defined as the empirical coverage of the nominal 95% confidence interval predicted by MC Dropout. Specifically, for each test sample and each time step, repeated stochastic forward passes with activated dropout produce a predictive mean $\mu_{i,t}$ and standard deviation $\sigma_{i,t}$. The corresponding confidence interval is constructed as $[\mu_{i,t}-1.96\sigma_{i,t}, \mu_{i,t}+1.96\sigma_{i,t}]$. The uncertainty coverage is then calculated as the proportion of all sample-time points whose true stress values fall within this interval, which reflects how well the predicted uncertainty intervals cover the true response.

As shown in Fig. A1(a-b), the predictive accuracy remains relatively stable for dropout rates between 0.1 and 0.4. The highest R^2 is obtained at 0.1, while the lowest MSE is achieved at 0.2. The result at 0.3 remains close to the best-performing cases, indicating that the point-prediction accuracy is largely preserved. By contrast, the uncertainty coverage increases monotonically from about 71% at 0.1 to about 89% at 0.5, as shown in Fig. A1(c), suggesting that larger dropout rates produce wider and more conservative uncertainty intervals. However, when the dropout rate reaches 0.5, the prediction accuracy deteriorates noticeably, as evidenced by the clear drop in R^2 and the sharp increase in MSE.

These results indicate a trade-off between predictive accuracy and uncertainty coverage. A small dropout rate tends to favor point prediction, while a large dropout rate improves coverage at the cost of over-regularization and reduced accuracy. Therefore, a dropout rate of 0.3 was adopted in this study as a balanced compromise: it maintains near-optimal prediction accuracy while already providing a substantial improvement in uncertainty coverage.

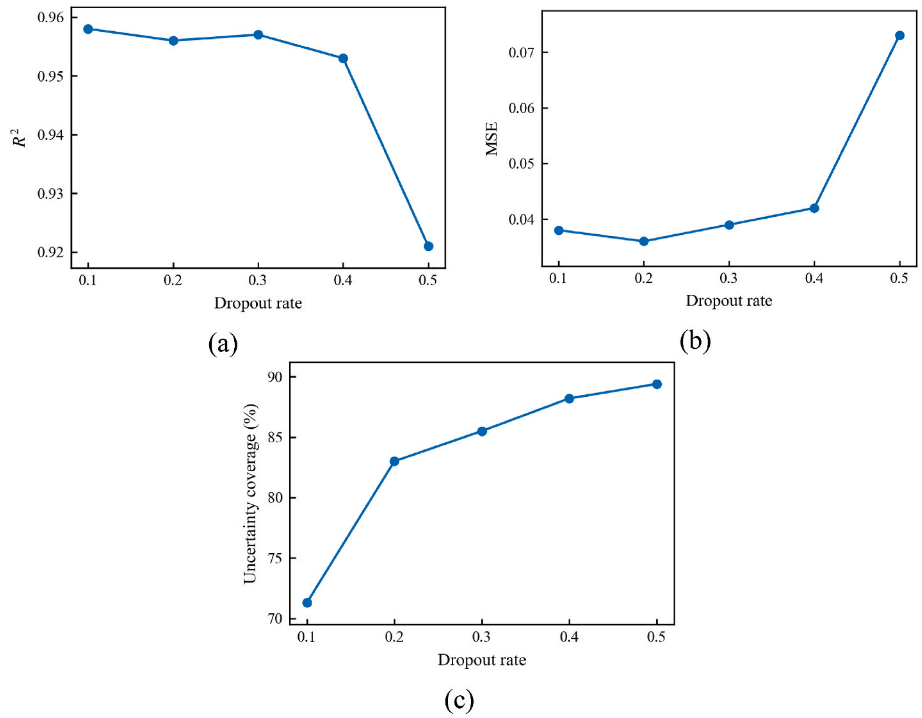

(a) (b) (c)

Fig. A1. Parametric study of the effects of dropout rate on R^2 (a), MSE (b), and uncertainty coverage (c).

Data availability

Data will be made available on request.

References

Afroz, S., Nguyen, Q.D., Zhang, Y., Kim, T., Castel, A., 2022. Evaluation of cracking potential parameters for low to high grade concrete with fly ash or slag. Constr. Build. Mater. 350, 128891. https://doi.org/10.1016/j.conbuildmat.2022.128891.

Azenha, M., Sousa, C., Faria, R., Neves, A., 2011. Thermo–hygro–mechanical modelling of self-induced stresses during the service life of RC structures. Eng. Struct. 33, 3442–3453. https://doi.org/10.1016/j.engstruct.2011.07.008.

Azenha, M., Leitão, L., Granja, J.L., de Sousa, C., Faria, R., Barros, J.A.O., 2017. Experimental validation of a framework for hygro-mechanical simulation of self-induced stresses in concrete. Cement Concr. Compos. 80, 41–54. https://doi.org/10.1016/j.cemconcomp.2017.02.008.

Azenha, M., Kanavaris, F., Schlicke, D., Jędrzejewska, A., Benboudjema, F., Honorio, T., Šmilauer, V., Serra, C., Forth, J., Riding, K., Khadka, B., Sousa, C., Briffaut, M., Lacarrière, L., Koenders, E., Kanstad, T., Klausen, A., Torrenti, J.M., Fairbairn, E.M.R., 2021. Recommendations of RILEM TC 287-CCS: thermo-chemo-mechanical modelling of massive concrete structures towards cracking risk assessment. Mater. Struct. /Materiaux et Constructions 54, 135. https://doi.org/10.1617/s11527-021-01732-8.

Bayar, G., Bilir, T., 2019. A novel study for the estimation of crack propagation in concrete using machine learning algorithms. Constr. Build. Mater. 215, 670–685. https://doi.org/10.1016/J.CONBUILDMAT.2019.04.227.

Bažant, Z.P., Jirásek, M., 2018. Creep and Hygrothermal Effects in Concrete Structures. Springer Netherlands, Dordrecht. https://doi.org/10.1007/978-94-024-1138-6.

Bazant, Z.P., Kaplan, M.F., 1996. Concrete at High Temperatures: Material Properties and Mathematical Models.

Bazant, Z.P., Wu, S.T., 1974. Rate-Type Creep Law of Aging Concrete Based on Maxwell Chain ER(t r).

Bentz, D.P., 2008. A review of early-age properties of cement-based materials. Cement Concr. Res. 38, 196–204. https://doi.org/10.1016/j.cemconres.2007.09.005.

Boulay, C., Staquet, S., Delsaute, B., Carette, J., Crespini, M., Yazoghli-Marzouk, O., Merliot, É., Ramanich, S., 2014. How to monitor the modulus of elasticity of concrete, automatically since the earliest age? Mater. Struct. /Materiaux et Constructions 47, 141–155. https://doi.org/10.1617/s11527-013-0051-3.

Breiman, L., 1996. Bagging predictors. Mach. Learn. 24, 123–140. https://doi.org/10.1007/BF00058655.

Briffaut, M., Benboudjema, F., D'Aloia, L., 2016. Effect of fibres on early age cracking of concrete tunnel lining. Part I: laboratory ring test. Tunn. Undergr. Space Technol. 59, 215–220. https://doi.org/10.1016/J.TUST.2016.07.016.

Cai, R., Han, T., Liao, W., Huang, J., Li, D., Kumar, A., Ma, H., 2020. Prediction of surface chloride concentration of marine concrete using ensemble machine learning. Cement Concr. Res. 136, 106164. https://doi.org/10.1016/j.cemconres.2020.106164.

Cervera, M., Oliver, J., Prato, T., 1999a. Thermo-chemo-mechanical model for concrete. II: damage and creep. J. Eng. Mech. 125, 1028–1039. https://doi.org/10.1061/(ASCE)0733-9399(1999)125:9(1028).

Cervera, M., Oliver, J., Prato, T., 1999b. Thermo-chemo-mechanical model for concrete. I: hydration and aging. J. Eng. Mech. 125, 1018–1027. https://doi.org/10.1061/(ASCE)0733-9399(1999)125:9(1018).

Chen, T., Guestrin, C., 2016. XGBoost. In: Proceedings of the 22nd ACM SIGKDD International Conference on Knowledge Discovery and Data Mining. ACM, New York, NY, USA, pp. 785–794. https://doi.org/10.1145/2939672.2939785.

Chung, J., Gulcehre, C., Cho, K., Bengio, Y., 2014. Empirical Evaluation of Gated Recurrent Neural Networks on Sequence Modeling. https://doi.org/10.48550/ARXIV.1412.3555.

Delsaute, B., Boulay, C., Staquet, S., 2016. Creep testing of concrete since setting time by means of permanent and repeated minute-long loadings. Cement Concr. Compos. 73, 75–88. https://doi.org/10.1016/J.CEMCONCOMP.2016.07.005.

Di Luzio, G., Cusatis, G., 2009a. Hygro-thermo-chemical modeling of high performance concrete. I: theory. Cement Concr. Compos. 31, 301–308. https://doi.org/10.1016/J.CEMCONCOMP.2009.02.015.

Di Luzio, G., Cusatis, G., 2009b. Hygro-thermo-chemical modeling of high-performance concrete. II: numerical implementation, calibration, and validation. Cement Concr. Compos. 31, 309–324. https://doi.org/10.1016/J.CEMCONCOMP.2009.02.016.

Di Luzio, G., Cedolin, L., Beltrami, C., 2020. Tridimensional long-term finite element analysis of reinforced concrete structures with rate-type creep approach. Appl. Sci. 10, 4772. https://doi.org/10.3390/app10144772.

Do, T.A., Le, B.-A., 2024. Machine learning approach for predicting early-age thermal cracking potential in concrete bridge piers. Forc. Mech. 17, 100297. https://doi.org/10.1016/j.finmec.2024.100297.

Echard, B., Gayton, N., Lemaire, M., 2011. AK-MCS: an active learning reliability method combining Kriging and Monte Carlo simulation. Struct. Saf. 33, 145–154. https://doi.org/10.1016/j.strusafe.2011.01.002.

Fairbairn, E.M.R., Azenha, M. (Eds.), 2019. Thermal Cracking of Massive Concrete Structures. Springer International Publishing, Cham. https://doi.org/10.1007/978-3-319-76617-1.

Fan, Y., Liu, J., Tao, Y., Sun, Y., Li, Z., Li, J., Wang, K., Ma, J., Fan, D., Xu, L., 2026. A transfer-learning framework to alleviate data scarcity in cross-slope wind pressure modeling. Results Eng. 29, 109376. https://doi.org/10.1016/j.rineng.2026.109376.

Faria, R., Azenha, M., Figueiras, J.A., 2006. Modelling of concrete at early ages: application to an externally restrained slab. Cement Concr. Compos. 28, 572–585. https://doi.org/10.1016/j.cemconcomp.2006.02.012.

Gal, Y., Ghahramani, Z., 2016. Dropout as a bayesian approximation: representing model uncertainty in deep learning. https://doi.org/10.48550/arXiv.1506.02142.

Gawin, D., Pesavento, F., Schrefler, B.A., 2006a. Hygro-thermo-chemo-mechanical modelling of concrete at early ages and beyond. Part II: shrinkage and creep of concrete. Int. J. Numer. Methods Eng. 67, 332–363. https://doi.org/10.1002/nme.1636.

Gawin, D., Pesavento, F., Schrefler, B.A., 2006b. Hygro-thermo-chemo-mechanical modelling of concrete at early ages and beyond. Part I: hydration and hygro-thermal phenomena. Int. J. Numer. Methods Eng. 67, 299–331. https://doi.org/10.1002/nme.1615.

Han, T., Siddique, A., Khayat, K., Huang, J., Kumar, A., 2020. An ensemble machine learning approach for prediction and optimization of modulus of elasticity of recycled aggregate concrete. Constr. Build. Mater. 244, 118271. https://doi.org/10.1016/J.CONBUILDMAT.2020.118271.

Hansen P., F., Pedersen, J., 1977. Maturity computer for controlled curing and hardening of concrete. Nordisk Betong 1, 19–34.

Hoffman, J.D., Hoffman, J.D., Frankel, S., 2018. Numerical Methods for Engineers and Scientists. CRC Press. https://doi.org/10.1201/9781315274508.

Hubler, M.H., Wendner, R., Bažant, Z.P., 2015. Comprehensive database for concrete creep and shrinkage: analysis and recommendations for testing and recording. ACI Mater. J. 112, 547–558. https://doi.org/10.14359/51687452.

International Federation for Structural Concrete (fib), 2013. Fib Model Code for Concrete Structures 2010. Ernst & Sohn, Wiley, Berlin, Germany.

Irfan-ul-Hassan, M., Pichler, B., Reihsner, R., Hellmich, Ch, 2016. Elastic and creep properties of young cement paste, as determined from hourly repeated minute-long quasi-static tests. Cement Concr. Res. 82, 36–49. https://doi.org/10.1016/j.cemconres.2015.11.007.

Jędrzejewska, A., Kanavaris, F., Zych, M., Schlicke, D., Azenha, M., 2020. Experiences on early age cracking of wall-on-slab concrete structures. Structures 27, 2520–2549. https://doi.org/10.1016/j.istruc.2020.06.013.

Jones, D.R., Schonlau, M., Welch, W.J., 1998. Efficient global optimization of expensive black-box functions. J. Global Optim. 13, 455–492. https://doi.org/10.1023/A:1008306431147.

Kang, M.C., Yoo, D.Y., Gupta, R., 2021. Machine learning-based prediction for compressive and flexural strengths of steel fiber-reinforced concrete. Constr. Build. Mater. 266, 121117. https://doi.org/10.1016/J.CONBUILDMAT.2020.121117.

Ke, G., Meng, Q., Finley, T., Wang, T., Chen, W., Ma, W., Ye, Q., Liu, T.Y., 2017. LightGBM: a highly efficient gradient boosting decision tree. In: Advances in Neural Information Processing Systems, pp. 3149–3157.

Klausen, A.E., 2016. Early Age Crack Assessment of Concrete Structures, Experimental Determination of Decisive Parameters. NTNU.

Klausen, A.E., Kanstad, T., Bjøntegaard, Ø., 2019. Hardening concrete exposed to realistic curing temperature regimes and restraint conditions: advanced testing and design methodology. Adv. Mater. Sci. Eng. 2019. https://doi.org/10.1155/2019/9071034.

Klausen, A.E., Kanstad, T., Bjøntegaard, Ø., 2022. The cracking risk of hardening concrete exposed to realistic curing temperature regimes and restraint conditions – experimental investigations of important parameters. Constr. Build. Mater. 338, 127662. https://doi.org/10.1016/J.CONBUILDMAT.2022.127662.

Klemczak, B., Batog, M., Giergiczny, Z., Żmij, A., 2018. Complex effect of concrete composition on the thermo-mechanical behaviour of mass concrete. Materials 11, 2207. https://doi.org/10.3390/ma11112207.

Lee, Y., Choi, M.-S., Yi, S.-T., Kim, J.-K., 2009. Experimental study on the convective heat transfer coefficient of early-age concrete. Cement Concr. Compos. 31, 60–71. https://doi.org/10.1016/j.cemconcomp.2008.09.009.

Li, H., Wang, S., 2025. A chemo-thermo-mechanical coupled phase-field model for complex early-age concrete mesoscale fracture simulations. Int. J. Solid Struct. 314, 113340. https://doi.org/10.1016/j.ijsolstr.2025.113340.

Li, Z., Liang, X., Liu, C., Liang, M., van Breugel, K., Ye, G., 2022. Thermal deformation and stress of alkali-activated slag concrete under semi-adiabatic condition: experiments and simulations. Cement Concr. Res. 159, 106887. https://doi.org/10.1016/j.cemconres.2022.106887.

Li, Z., Xu, J., Liang, M., Ye, G., Ou, J., 2025. Quantifying the early-age viscoelastic properties of alkali activated slag concrete using repeated minutes-long creep tests. RILEM Tech. Lett. 9, 106–116. https://doi.org/10.21809/rilemtechlett.2024.204.

Liang, M., 2024. Stress Evolution in Early-Age Cementitious Materials Considering Autogenous Deformation and Creep: New Experimental and Modelling Techniques. Delft University of Technology. https://doi.org/10.4233/UUID:270173E7-6CE6-4A71-AC42-79EAB09CCE5F.

Liang, M., Chang, Z., He, S., Chen, Y., Gan, Y., Schlangen, E., Šavija, B., 2022a. Predicting early-age stress evolution in restrained concrete by thermo-chemo-mechanical model and active ensemble learning. Comput. Aided Civ. Infrastruct. Eng. 37, 1809–1833. https://doi.org/10.1111/mice.12915.

Liang, M., Li, Z., He, S., Chang, Z., Gan, Y., Schlangen, E., Šavija, B., 2022b. Stress evolution in restrained GGBFS concrete due to autogenous deformation: bayesian optimization of aging creep. Constr. Build. Mater. 324, 126690. https://doi.org/10.1016/J.CONBUILDMAT.2022.126690.

Liang, M., Chang, Z., Wan, Z., Gan, Y., Schlangen, E., Šavija, B., 2022c. Interpretable ensemble-machine-learning models for predicting creep behavior of concrete. Cement Concr. Compos. 125, 104295. https://doi.org/10.1016/J.CEMCONCOMP.2021.104295.

Liang, M., Chang, Z., Zhang, Y., Cheng, H., He, S., Schlangen, E., Šavija, B., 2023a. Autogenous deformation induced- stress evolution in high-volume GGBFS concrete:

Macro-scale behavior and micro-scale origin. Constr. Build. Mater. 370, 130663. https://doi.org/10.1016/j.conbuildmat.2023.130663.

Liang, M., Schlangen, E., Šavija, B., 2023b. Bayesian inverse modelling of early-age stress evolution in GGBFS concrete due to autogenous deformation and aging creep, 207–217. https://doi.org/10.1007/978-3-031-07746-3_21.

Liang, M., Xie, J., He, S., Chen, Y., Schlangen, E., Šavija, B., 2024a. Autogenous deformation-induced stress evolution in cementitious materials considering viscoelastic properties: a review of experiments and models. Dev. Built Environ. 17, 100356. https://doi.org/10.1016/j.dibe.2024.100356.

Liang, M., Chang, Z., Holthuizen, P., Chen, Y., He, S., Schlangen, E., Šavija, B., 2024b. Efficiently assessing the early-age cracking risk of cementitious materials with a mini temperature stress testing machine. Cement Concr. Compos. 153, 105710. https://doi.org/10.1016/j.cemconcomp.2024.105710.

Liang, M., Luzio, G.D., Schlangen, E., Šavija, B., 2024c. Experimentally informed modeling of the early-age stress evolution in cementitious materials using exponential conversion from creep to relaxation. Computer-Aided Civil and Infrastructure Engineering. https://doi.org/10.1111/mice.13156.

Liang, M., Liu, C., Liang, X., Chang, Z., Schlangen, E., Šavija, B., 2024d. Effects of temperature on autogenous deformation and early-age stress evolution in cement pastes with low water to cement ratio. Constr. Build. Mater. 411, 134752. https://doi.org/10.1016/j.conbuildmat.2023.134752.

Liu, Y., Schindler, A.K., 2020. Finite-element modeling of early-age concrete stress development. J. Mater. Civ. Eng. 32, 04019338. https://doi.org/10.1061/(asce)mt.1943-5533.0002988.

Liu, J., Wang, S., Chen, K., Wang, K., Fan, Y., Wang, Q., 2026. Synthetic data augmentation and Integrated prediction framework for low-carbon recycled concrete: leveraging CTGAN and multiple ML models stacking. J. Clean. Prod. 543, 147599. https://doi.org/10.1016/j.jclepro.2026.147599.

Loh, W.-L., 1996. On Latin hypercube sampling. Ann. Stat. 24, 2058–2080. https://doi.org/10.1214/aos/1069362310.

Lura, P., Jensen, O.M., Weiss, J., 2009. Cracking in cement paste induced by autogenous shrinkage. Mater. Struct. /Materiaux et Constructions 42, 1089–1099. https://doi.org/10.1617/s11527-008-9445-z.

Mao, J., Liang, N., Liu, X., Zhong, Z., Zhou, C., 2023. Investigation on early-age cracking resistance of basalt-polypropylene fiber reinforced concrete in restrained ring tests. J. Build. Eng. 70, 106155. https://doi.org/10.1016/j.jobe.2023.106155.

Moustapha, M., Marelli, S., Sudret, B., 2022. Active learning for structural reliability: survey, general framework and benchmark. Struct. Saf., 102174 https://doi.org/10.1016/J.STRUSAFE.2021.102174.

Nguyen, D.H., Nguyen, V.T., Lura, P., Dao, V.T.N., 2019. Temperature-stress testing machine – a state-of-the-art design and its unique applications in concrete research. Cement Concr. Compos. 102, 28–38. https://doi.org/10.1016/J.CEMCONCOMP.2019.04.019.

Nguyen, H., Vu, T., Vo, T.P., Thai, H.-T., 2021. Efficient machine learning models for prediction of concrete strengths. Constr. Build. Mater. 266, 120950. https://doi.org/10.1016/j.conbuildmat.2020.120950.

Ou, G., Lin, Z., Kishi, T., 2023. The practical application of a self-developed temperature stress testing machine in development of expansive concrete blended with calcium sulfoaluminate additives. Cement Concr. Res. 164, 107045. https://doi.org/10.1016/j.cemconres.2022.107045.

Pantazopoulou, S.J., Mills, R.H., 1995. Microstructural aspects of the mechanical response of plain concrete. ACI Mater. J. 92, 605–616. https://doi.org/10.14359/9780.

Pasparakis, G.D., Graham-Brady, L., Shields, M.D., 2025. Bayesian neural networks for predicting uncertainty in full-field material response. Comput. Methods Appl. Mech. Eng. 433, 117486. https://doi.org/10.1016/j.cma.2024.117486.

Pedregosa, F., Varoquaux, G., Gramfort, A., Michel, V., Thirion, B., Grisel, O., Blondel, M., Müller, A., Nothman, J., Louppe, G., Prettenhofer, P., Weiss, R., Dubourg, V., Vanderplas, J., Passos, A., Cournapeau, D., Brucher, M., Perrot, M., Duchesnay, É., 2012. Scikit-Learn: Machine Learning in Python.

Rasmussen, C.Edward, Williams, C.K.I., 2006. Gaussian Processes for Machine Learning. MIT Press.

Semianiuk, V., Tur, V., Herrador, M.F., Paredes G, M., 2017. Early age strains and self-stresses of expansive concrete members under uniaxial restraint conditions. Constr. Build. Mater. 131, 39–49. https://doi.org/10.1016/J.CONBUILDMAT.2016.11.008.

Shen, D., Jiang, J., Shen, J., Yao, P., Jiang, G., 2016. Influence of curing temperature on autogenous shrinkage and cracking resistance of high-performance concrete at an early age. Constr. Build. Mater. 103, 67–76. https://doi.org/10.1016/J.CONBUILDMAT.2015.11.039.

Shen, D., Jiang, J., Wang, W., Shen, J., Jiang, G., 2017. Tensile creep and cracking resistance of concrete with different water-to-cement ratios at early age. Constr. Build. Mater. 146, 410–418. https://doi.org/10.1016/j.conbuildmat.2017.04.056.

Shen, S.-L., Wu, H., Zhou, A., 2025. Physics-informed neural network modelling of uplift behaviour of segmental linings during shield tunnelling. J. Rock Mech. Geotech. Eng. 17, 7515–7527. https://doi.org/10.1016/j.jrmge.2025.08.001.

Stute, B., Krupp, V., von Lieres, E., 2013. Performance of iterative equation solvers for mass transfer problems in three-dimensional sphere packings in COMSOL. Simulat. Model. Pract. Theor. 33, 115–131. https://doi.org/10.1016/j.simpat.2012.10.004.

Taylor, H.F.W., 1997. Cement Chemistry. Thomas Telford Publishing. https://doi.org/10.1680/cc.25929.

Tomar, A., Burton, H.V., 2021. Active learning method for risk assessment of distributed infrastructure systems. Comput. Aided Civ. Infrastruct. Eng. 36, 438–452. https://doi.org/10.1111/mice.12665.

Ulm, F.-J., Coussy, O., 1995. Modeling of thermochemomechanical couplings of concrete at early ages. J. Eng. Mech. 121, 785–794. https://doi.org/10.1061/(ASCE)0733-9399(1995)121:7(785).

Van Breugel, K., 1980. Relaxation of Young Concrete.

van Breugel, K., 1991. Simulation of Hydration and Formation of Structure in Hardening Cement-based Materials. TU Delft.

Waltz, R.A., Morales, J.L., Nocedal, J., Orban, D., 2006. An interior algorithm for nonlinear optimization that combines line search and trust region steps. Math. Program. 107, 391–408. https://doi.org/10.1007/s10107-004-0560-5.

Wan, Z., Xu, Y., Šavija, B., 2021. On the use of machine learning models for prediction of compressive strength of concrete: influence of dimensionality reduction on the model performance. Materials 14, 713. https://doi.org/10.3390/ma14040713.

Wang, K., Shen, T., Liu, J., Wang, S., Bao, X., Wei, J., Hu, W., Xu, L., 2025. Exploration of computational formulations for wind-induced interference effects on high-rise buildings via Kolmogorov–Arnold networks. Dev. Built Environ. 24, 100770. https://doi.org/10.1016/j.dibe.2025.100770.

Wang, S., Chen, Y., Gong, F., Fan, Y., Huang, B.-T., Zhang, H., 2026. Intelligent framework of temperature and humidity field coupling of early-age concrete considering hydration based on physics informed neural network. Int. Commun. Heat Mass Tran. 172, 110203. https://doi.org/10.1016/j.icheatmasstransfer.2025.110203.

Wei, Y., Liang, S., Guo, W., Hansen, W., 2017. Stress prediction in very early-age concrete subject to restraint under varying temperature histories. Cement Concr. Compos. 83, 45–56. https://doi.org/10.1016/j.cemconcomp.2017.07.006.

Wittmann, F., 1974. Bestimmung Physikalischer Eigenschaften Des Zementsteins.

Xin, J., Liu, Y., Zhang, G., Wang, Z., Yang, N., Qiao, Y., Wang, J., 2021. Comparison of thermal cracking potential evaluation criteria for mass concrete structures. Mater. Struct. 54, 243. https://doi.org/10.1617/s11527-021-01840-5.

Xu, C., Cao, B.T., Yuan, Y., Meschke, G., 2024. A multi-fidelity deep operator network (DeepONet) for fusing simulation and monitoring data: application to real-time settlement prediction during tunnel construction. Eng. Appl. Artif. Intell. 133, 108156. https://doi.org/10.1016/j.engappai.2024.108156.

Xu, Q., Zhang, C., Geng, S., Wang, S., Li, J., Liu, J., Chen, K., Zhang, Y., Xu, L., 2025. An explainable ensemble learning framework for flexible pavement roughness prediction under multi-climate stressors. Case Stud. Constr. Mater. 23, e05402. https://doi.org/10.1016/j.cscm.2025.e05402.

Zhang, Y., Xi, M., Liu, J., Wang, W., Lyu, X., 2025a. Axial compressive capacity prediction of coal gangue concrete-filled steel tube stub columns: genetic programming-augmented code calibration and Bayesian-optimized machine learning. Structures 80, 110119. https://doi.org/10.1016/j.istruc.2025.110119.

Zhang, Y., Wang, Z., Xi, M., Zhao, Y., Liu, J., 2025b. Data-driven prediction of residual flexural capacity in corroded RC beams using PSO and GA-optimized CatBoost ensemble models. Eng. Res. Express 7, 035129. https://doi.org/10.1088/2631-8695/adfcb3.

Zhang, Y., Wang, Z., Liu, J., Li, Y., Huang, Z., Yu, X., 2026a. A metaheuristic-driven categorical boosting framework with interpretability for high-precision prediction of mechanical properties in corroded reinforced concrete beams. Eng. Appl. Artif. Intell. 163, 112804. https://doi.org/10.1016/j.engappai.2025.112804.

Zhang, Y., Wang, H., Liu, J., Liu, F., Lv, X., 2026b. Intelligent structural design of composite concrete-encased steel columns based on hybrid machine learning and multiobjective optimization. Struct. Concr. 27, 49–72. https://doi.org/10.1002/suco.70292.

Zhao, H., Jiang, K., Yang, R., Tang, Y., Liu, J., 2020. Experimental and theoretical analysis on coupled effect of hydration, temperature and humidity in early-age cement-based materials. Int. J. Heat Mass Tran. 146, 118784. https://doi.org/10.1016/j.ijheatmasstransfer.2019.118784.

Zhao, H., Jiang, K., Hong, B., Yang, R., Xu, W., Tian, Q., Liu, J., 2021. Experimental and numerical analysis on coupled hygro-thermo-chemo-mechanical effect in early-age concrete. J. Mater. Civ. Eng. 33, 04021064. https://doi.org/10.1061/(ASCE)MT.1943-5533.0003666.

Zhu, H., Li, Q., Hu, Y., 2017. Self-developed testing system for determining the temperature behavior of concrete. Materials 10. https://doi.org/10.3390/ma10040419.

Zhu, H., Li, Q., Hu, Y., Ma, R., 2018. Double feedback control method for determining early-age restrained creep of concrete using a temperature stress testing machine. Materials 11. https://doi.org/10.3390/ma11071079.